Optical Engineering

OpticalEngineering.SPIEDigitalLibrary.org

Generation and decomposition of scalar and vector modes carrying orbital angular momentum: a review

Srinivas Pachava
Raghu Dharmavarapu
Anand Vijayakumar
Sruthy Jayakumar
Amogh Manthalkar
Awakash Dixit
Nirmal K. Viswanathan
Balaji Srinivasan
Shanti Bhattacharya

SPIE.

Srinivas Pachava, Raghu Dharmavarapu, Anand Vijayakumar, Sruthy Jayakumar, Amogh Manthalkar, Awakash Dixit, Nirmal K. Viswanathan, Balaji Srinivasan, Shanti Bhattacharya, "Generation and decomposition of scalar and vector modes carrying orbital angular momentum: a review," *Opt. Eng.* **59**(4), 041205 (2019), doi: 10.1117/1.OE.59.4.041205.

REVIEW

Generation and decomposition of scalar and vector modes carrying orbital angular momentum: a review

Srinivas Pachava,[a,†] Raghu Dharmavarapu,[a,b,†] Anand Vijayakumar,[a,b] Sruthy Jayakumar,[a] Amogh Manthalkar,[a] Awakash Dixit,[a] Nirmal K. Viswanathan,[c,*] Balaji Srinivasan,[a,*] and Shanti Bhattacharya[a,*]

[a]Indian Institute of Technology Madras, Department of Electrical Engineering, Chennai, Tamil Nadu, India

[b]Swinburne University of Technology, Centre for Micro-Photonics, Faculty of Science, Engineering and Technology, Hawthorn, Victoria, Australia

[c]University of Hyderabad, School of Physics, Hyderabad, Telangana, India

Abstract. Orbital angular momentum (OAM), one of the most recently discovered degrees of freedom of light beam field has fundamentally revolutionized optical physics and its technological capabilities. Optical beams with OAM have enabled a large variety of applications, including super-resolution imaging, optical trapping, classical and quantum optical communication, and quantum computing, to mention a few. To enable these and several other emerging applications, optical beams with OAM have been generated using a variety of methods and technologies, such as a simple astigmatic lens pair, one-/two-dimensional holographic optical elements, three-dimensional spiral phase plates, optical fibers, and recent entrants such as metasurfaces. All these techniques achieve spatial light modulation and can be implemented with either passive elements or active devices, such as liquid crystal on silicon and digital micromirror devices. Many of these devices and technologies are not only used for the generation of amplitude phase-polarization structured light beams but are also capable of analyzing them. We have attempted to encompass a wide variety of such technologies as well as a few emerging methodologies, broadly categorized into generation and detection protocols. We address the needs of scientists and engineers who desire to generate/detect OAM modes and are looking for the technique (active or passive) best suited for their application. [DOI: 10.1117/1.OE.59.4.041205]

Keywords: orbital angular momentum; spatial light modulators.

Paper 191359SSV received Sep. 27, 2019; accepted for publication Nov. 20, 2019; published online Dec. 12, 2019.

1 Introduction

The fact that light carries spin angular momentum (SAM) of $\sigma\hbar$ ($\sigma = \pm 1$) was known as early as 1909, when Poynting demonstrated that a circularly polarized beam of light could cause a piece of birefringent material suspended on a thin wire to rotate about its center.[1] However, it was not until 1992 that Allen et al.[2] proved that an optical beam with azimuthal varying phase $\exp(il\phi)$ carries orbital angular momentum (OAM) of $l\hbar$ per photon, with l being the topological charge of the beam. The past three decades have seen tremendous growth of such optical beams from being a mere scientific curiosity to being a key enabler in a wide variety of cutting-edge applications, such as super-resolution imaging, optical trapping, and classical and quantum optical communications. In all these applications, the first step is the generation of an OAM mode. Experimentally, there are numerous methods to generate the desired OAM modes.[3–5] One of the first reports on the generation of OAM mode was simply using two cylindrical lenses.[6]

*Address all correspondence to Shanti Bhattacharya, E-mail: shanti@ee.iitm.ac.in; Balaji Srinivasan, E-mail: balajis@ee.iitm.ac.in; Nirmal Viswanathan, E-mail: nirmalsp@uohyd.ac.in

†These authors contributed equally to this work.

Since then, there has been tremendous growth in this field, and the current state of the art includes several different design techniques such as binary holographic optical designs, spiral phase plate (SPP) designs, and planar metasurface designs. In general, OAM mode generation is achieved by modulation of one or more of the incident light beam's characteristics through an optical element fabricated lithographically using electron beam, ion beam, and/or photolithography, or by using active devices, such as liquid crystal on silicon (LCoS)-based spatial light modulators (SLMs) and digital micromirror devices (DMDs).

In this paper, we discuss the various widely used phase-modulation- and amplitude-modulation-based approaches for generating the desired OAM modes using both passive and active optical elements. In addition to the scalar OAM mode generation mentioned above, SLMs are also used extensively to manipulate the polarization and intensity degrees of freedom (DoFs) of a light beam to generate vector modes of light beam—fields without and with angular momentum (AM) from standard laser source. Generation of phase-polarization structured light beam fields in two-dimensional (2-D) is a growing field in optical science and its applications span research areas, including polarization imaging, data encoding, and polarization multiplexing. This is also discussed in the first section. Second, in certain applications, such as optical communication, detection of specific OAM modes in a precise manner is important in order to demodulate the information carried by the different modes. The methods for detection and sorting of OAM modes will also be analyzed and reviewed in this paper.

1.1 *Characteristics of Orbital Angular Momentum Modes*

Optical beams carrying OAM typically exhibit helical wavefronts. The pitch and handedness of the helix determine the topological charge and type (positive/negative) of the OAM beam.[7] Various solutions of the Helmholtz wave equation can result in different kinds of beams that carry OAM. The differences arise based on the geometry or conditions that are used to solve the wave equation. Examples of some of the solutions with an OAM component are Laguerre–Gaussian (LG) modes,[2] Bessel modes,[8] Mathieu modes,[9] Ince–Gaussian modes,[10] and hypergeometric-Gaussian modes.[11,12]

The solutions of the paraxial wave equation in cylindrical coordinates (ρ, ϕ, z) have a transverse scalar electric field given as

$$\mathrm{LG}_{lp}(\rho,\phi,z) = C_{lp}^{\mathrm{LG}} \exp\left(\frac{-\rho^2}{w^2}\right)\left(\frac{\sqrt{2}\rho}{w}\right)^{|l|} \mathrm{LG}_p^{|l|}\left(\frac{2\rho^2}{w^2}\right) \exp\left(il\phi + \frac{ik\rho^2}{2R} - i\psi_G\right), \tag{1}$$

with

$$R = (z_R^2 + z^2)/z, \tag{2}$$

$$kw^2 = 2(z_R^2 + z^2)/z_R, \tag{3}$$

$$\psi_G = (2p + |l| + 1)\tan^{-1}(z/z_R), \tag{4}$$

where C_{lp}^{LG} is the normalization constant, z_R is the Rayleigh range, ψ_G is the Gouy phase, w is the beam radius, R is the radius of the spherical wavefront, $k = 2\pi/\lambda$ is the wave number, LG is the Laguerre polynomial, and l and p are the azimuthal and radial modal numbers. These modes are also called LG modes. The $\exp(il\phi)$ term denotes the azimuthal phase variation, because of which, the beam exhibits OAM of $l\hbar$ per photon. The term $\exp(-ik\rho^2/2R)$ represents the spherical wavefront structure of the beam. LG polynomials with variables l and p are orthogonal to each other. Therefore, LG modes with beam waist w and l and p modal numbers form a complete orthogonal basis set. The intensity and phase structures of LG modes with $-2 < l < 2$, $p = 0, 1$ are shown in Figs. 1 and 2. LG modes have a donut intensity structure if azimuthal number is $|l| > 0$. In general, LG modes have $p + 1$ rings in the intensity structure.

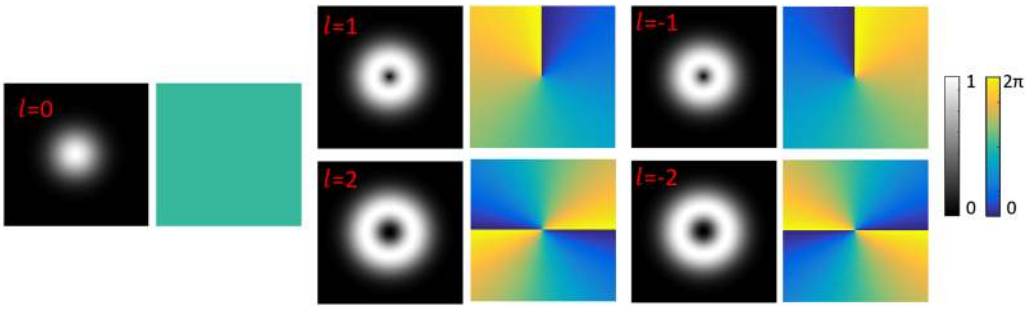

Fig. 1 Intensity (grey) and phase structures (coloured) of LG modes with azimuthal numbers $l = 0, \pm 1, \pm 2$ and $p = 0$.

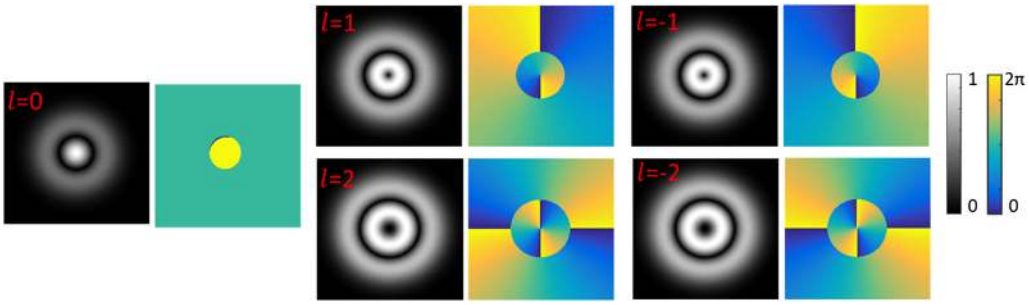

Fig. 2 Intensity (grey) and phase structures (coloured) of LG modes with azimuthal numbers $l = 0, \pm 1, \pm 2$ and $p = 1$.

1.2 *Applications of Orbital Angular Momentum Modes*

In Sec. 1, we briefly mentioned some of the applications of OAM modes. We discuss them in more detail in this section. In optical communications, the need for supporting higher data rates in a single optical fiber has led researchers to explore the path of mode division multiplexing (MDM). In conventional MDM, data are encoded in spatially orthogonal light beams based on the linearly polarized (LP) modes. The primary limitation with LP mode-based MDM communications is intermodal coupling, which essentially increases cross talk and degrades the signal-to-noise ratio (SNR). To address this issue, several research groups are exploring the possibility of using OAM modes as they promise lower intermodal coupling.[13,14] It is to be noted that OAM modes are actually unapproximated solutions of the optical fiber and are hence called "true modes" of the fiber.[15,16]

Stimulated emission depletion microscopy is one of the most successful far-field imaging techniques, allowing access to resolution beyond the diffraction limit.[17] It uses a Gaussian-shaped beam to excite the fluorophore and a redshifted, spatially overlapped donut-shaped beam to deplete the fluorescence everywhere except at the dark center of the depletion beam. OAM modes with a donut intensity structure are the "perfect" candidates for such applications.[18,19]

Donut-shaped modes are also used in material processing, such as glass cutting, since the induced stress in the center of the irradiated area is minimal.[20] OAM modes have many diverse applications such as in optical trapping experiments to study biological interactions,[21] as a rotational sensor for the remote detection of spinning objects based on rotational Doppler shift of the modes;[22] in astronomy, where some of their properties are used in coronagraphs[23] and in quantum information processing to enlarge the information content that a qubit can transmit.[24]

1.3 *Need for Detection and Sorting of Orbital Angular Momentum Modes*

The need for higher data rate in optical communication has been met by various multiplexing schemes such as polarization division multiplexing, wavelength division multiplexing, and, as

mentioned already, MDM. The different spatial modes in MDM are utilized as information-carrying channels and are copropagated through the same communication medium (free space or fiber). OAM modes of different topological charges are orthogonal to each other and hence form a suitable basis set of nonoverlapping channels for MDM.[25,26] Even in cases where only a single mode carrying information was used, the very process of propagation, whether through free space or fiber could cause the mode to deteriorate and leak into other modes. In such cases, the signal received at the detector can be considered to comprise a set of superimposed OAM modes, and it is important to separate and quantify the modal weight of the various modes present in the resultant beam.[27] In such cases, it becomes necessary to multiplex and demultiplex a number of modes and hence this has become an important research area in recent times. In addition, quantifying the modal weights, commonly called modal decomposition, has potential applications in wavefront reconstruction,[28] beam quality measurement (M^2),[29] and in the fiber-to-fiber coupling process.[30]

2 Generation of Optical Beams Carrying Orbital Angular Momentum

Complex light refers to electromagnetic radiation whose inherent parameters such as intensity, phase, and polarization are manipulated to yield a specific structure. Depending upon the requirement, either one or more of the above parameters are customized and controlled.[31–40] Structuring the phase of light requires an optical element possessing a thickness or refractive index modulation or both.[42] A higher thickness/refractive index results in a longer optical path, whereas lower values result in shorter optical paths. The result is a differential phase retardation across the beam, which is given as $\Delta\Phi(x,y) = 2\pi n\Delta t(x,y)/\lambda[\simeq 2\pi t\Delta n(x,y)/\lambda]$, where n is the refractive index of the medium, λ is the wavelength, and t is the thickness. An example of a transverse phase modulation is depicted in Fig. 3. Clearly, advanced manufacturing techniques are required in order to sculpt the desired surface relief pattern. Typical examples of such phase-manipulating SLMs include holographic optical elements (HOEs), refractive/diffractive optical elements (DOEs), and dielectric metasurfaces. Such approaches are discussed in more detail in subsequent sections. While these elements constitute passive SLMs, it is interesting to note that the corresponding phase patterns may also be implemented using active SLMs, such as LCoS devices. The obvious advantages of such active devices are their flexibility and reconfigurability. However, such devices are relatively expensive and hence are more suited for niche applications that require switching between various phase patterns, as in the case of modal decomposition.

A relatively easier parameter to sculpt is the intensity distribution, where an SLM consisting of an amplitude mask with variable transmittivity values across the transverse plane is sufficient to generate a desired intensity function, as shown in Fig. 4.[33] A common example of such an approach is the use of a DMD, which is described in the subsequent section. It is interesting to

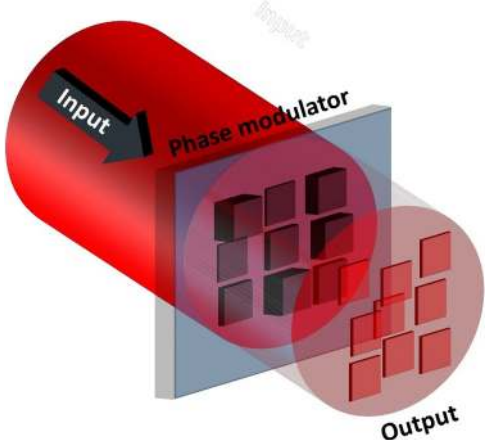

Fig. 3 Phase modulation of a light beam using an SLM with varying phase across the beam cross section.

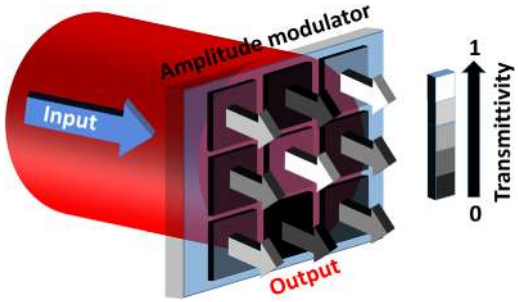

Fig. 4 Amplitude modulation of a light beam using a SLM with varying transmittivity across the beam cross-section.

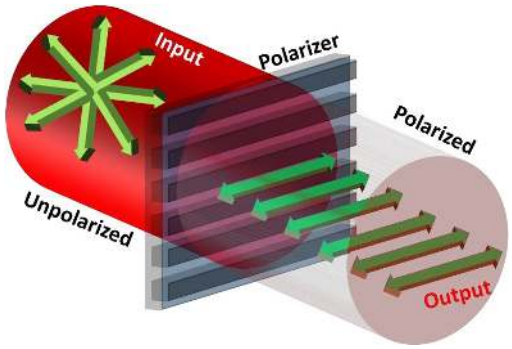

Fig. 5 Polarization modulation of a light beam using a polarizer.

note that although the DMD constitutes an amplitude-only manipulating device, it can be programmed to generate a desired phase distribution at some distance from the device.

Polarization modulation can be achieved using a polarizer, as shown in Fig. 5. For some applications, it is sufficient to modulate only one parameter such as amplitude or phase, whereas in other cases it is desirable to simultaneously modulate one or more parameters to produce an optical beam with particular structure.[43]

2.1 *Phase Modulation Approach*

In this section, various phase modulation-based schemes to generate beams with OAM are discussed. As mentioned in the previous section, a spatial variation of refractive index and/or thickness alters phase. Therefore, by this definition even refractive elements can be considered to be SLMs. While there are methods that use refractive elements, such as the work by Beijersbergen et al.[6] that generated high-order LG modes directly from a laser using cylindrical lenses as mode convertors, this review focuses mainly on spatial light modulation based on interferometric, diffractive, or metaoptics to generate OAM beams. The one refractive element that will be discussed in detail is the SPP, as it is often the starting point for designs carried out using these alternative phase methods.

2.1.1 *Generation using refractive spiral phase plate*

An SPP is a refractive element with a spiral thickness profile, as shown in Fig. 6. This element creates a complex wave with a spiral phase retardation.[44–46] One of the main advantages of using an SPP for generating a spiral wave is that the conversion efficiency can be close to 100%. However, the challenge lies in manufacturing a refractive element with a smooth variation in height. Therefore, in most implementations of the SPP, only an approximate version is fabricated.[47–52]

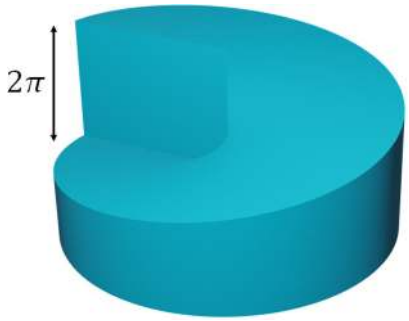

Fig. 6 SPP for generation of LG beam with $\ell = 1$.

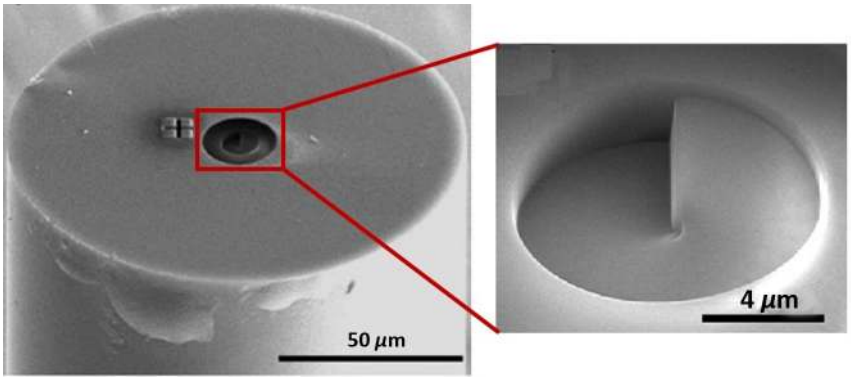

Fig. 7 Electron microscope image of SPP fabricated on the tip of an optical fiber (reprinted from Ref. 53).

Advances in focused ion beam milling technology enabled the fabrication of a refractive SPP directly on the tip of an optical fiber.[53] An electron beam microscope image of the fabricated element on a single-mode fiber (SMF) is shown in Fig. 7. Recent measurements on OAM modal purity using the modal decomposition method revealed that it is sufficient to have only three phase levels (for $\ell = 1$) instead of a continuous phase variation for the generation of a fundamental OAM mode ($\ell = 1,\ p = 0$) with a high modal purity.[54] However, further studies are necessary to understand the effect of such an approximation on other applications such as optical trapping and communication. In addition, when the topological charge increases, the number of phase levels required to achieve a good accuracy also increases, which brings back the fabrication challenge. For these reasons, the SPP is usually modified using some technique into a simpler version and fabricated, instead of the continuous spiral pattern. These methods will be discussed in subsequent sections.

2.1.2 *Generation using blazed and diffractive optical elements*

Methods used to design complex light-generating elements always result in a continuous phase pattern, which we have seen is hard to fabricate. Often the analog phase is converted to a blazed structure using a modulo 2π operation. In other words, sections that change the phase of light by 2π are removed. Blazed elements still have smooth curved sides, as shown on the left of Fig. 8, that are almost impossible to make with conventional lithography techniques.

One way of making approximate blazed elements is by quantizing the continuous phase into n discrete levels, resulting in what are called DOEs. These quantized phase profiles needs to be converted into GDSII format[55] in order to be fabricated with lithography tool. Theoretically, an eight-level quantization can give rise to an efficiency of 94.9% and a 16-level approximation to 98.7%.[56] However, it is still highly challenging to fabricate DOEs with more than two levels, as the process will require multiple lithography steps. The conversion from a blazed element to a binary (two-level) DOE is depicted in Fig. 8.

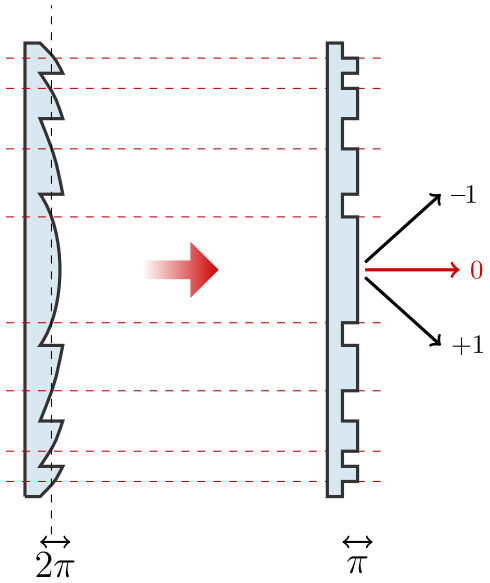

Fig. 8 Conversion from a Fresnel lens to a diffractive lens by quantizing the phase levels to binary levels (0 and π).

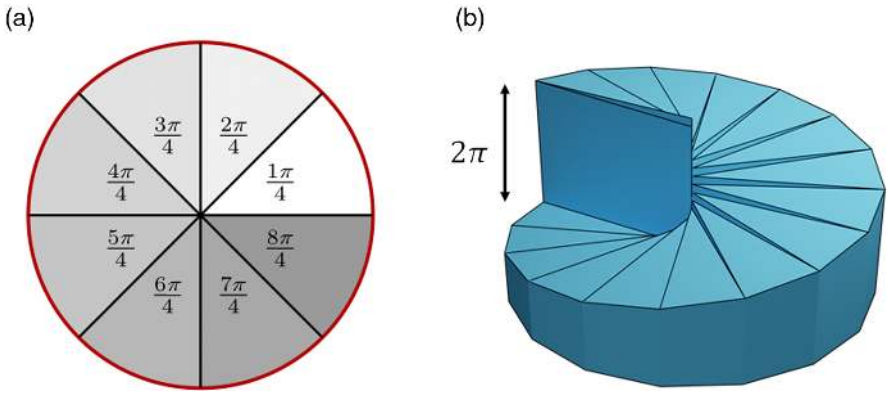

Fig. 9 (a) Top view of an eight-level SPP and (b) a 3-D view of a 16-level SPP.

An SPP can also be created as a diffractive element. However, an SPP of charge 1 would have only two levels and would not be an accurate representation of the actual element. In this case, the azimuthal phase is split into sectors, with each sector being of constant phase, as shown in Fig. 9, resulting in a multilevel phase element.

Binary DOEs are the easiest to fabricate and can also be mass-produced, which makes them affordable. It should be noted that the binarizing procedure decomposes the incoming field into its Fourier components in the Fourier plane resulting in the generation of several orders.[43] In the case of the SPP, the higher orders have higher topological charge values. This means that the efficiency (the fraction of power that goes into forming the desired beam) is poor. The first order will have at most 40.5% efficiency, for a binary element.

2.1.3 *Generation using holographic optical elements*

As mentioned in the previous section, fabrication of a refractive element can be challenging. Holographic techniques can be used to overcome these challenges. Holography is the science of recording and reconstructing three-dimensional (3-D) information of an object.[57–59] When used to generate complex light, interference is carried out between the desired (hard-to-fabricate) phase distribution and a simple reference beam. The resulting pattern is usually simpler to

fabricate. The hologram-recording process can be mathematically expressed as follows: two mutually coherent electromagnetic waves with complex amplitudes $\Psi_1(x,y) = A_1(x,y)\exp[j\Phi_1(x,y)]$ and $\Psi_2(x,y) = A_2(x,y)\exp[j\Phi_2(x,y)]$ are interfered to create a hologram, in which the relative phase difference is converted into an intensity distribution given as $I = C_1(x,y) + C_2(x,y)\exp\{j[\Phi_1(x,y) - \Phi_2(x,y)]\} + C_2(x,y)\exp\{-j[\Phi_1(x,y) - \Phi_2(x,y)]\}$, where $C_1(x,y) = |A_1(x,y)|^2 + |A_2(x,y)|^2$ and $C_2(x,y) = A_1(x,y)A_2(x,y)$. The terms $C_1(x,y)$ and $C_2(x,y)$ contain the information of the intensity of the two interfering waves, whereas the relative phase information $[\Phi_1(x,y) - \Phi_2(x,y)]$ is encoded in the second and third terms.

Early holography involved the use of photopolymers, dichromated gelatin, and photorefractive materials, as these materials were required to store the intensity variation.[57] The intensity was created using an experimental setup. However, after the development of computers, holography evolved into computer-generated and digital holography.[57–62] In computer-generated holography (CGH), the entire hologram-recording process is carried out computationally and is, therefore, aberration-free. In addition, it is possible to create any exotic phase distribution with only imagination being the limit. By creating complex amplitudes with uniform intensity, the above intensity distribution can be reduced to $I = C_1 + C_2\ \exp\{j[\Phi_1(x,y) - \Phi_2(x,y)]\} + C_2\ \exp\{-j[\Phi_1(x,y) - \Phi_2(x,y)]\}$. Consider the electromagnetic wave with a phase distribution $\Phi_1(x,y)$ as the reference wave. When its conjugate illuminates I, the following beams are generated: $\exp[-j\Phi_1(x,y)] \times (C_1 + C_2\ \exp\{j[\Phi_1(x,y) - \Phi_2(x,y)]\} + C_2\ \exp\{-j[\Phi_1(x,y) - \Phi_2(x,y)]\})$. This reduces to $\Psi_r = C_3\exp[j\Phi_1(x,y)] + C_4\exp[-j\Phi_2(x,y)] + C_4\exp\{-j[2\Phi_1(x,y) - \Phi_2(x,y)]\}$ upon simplification. If $\Phi_1(x,y)$ is a carrier wave given as $\exp[-j2\pi(\lambda)^{-1}(s_x x + s_y y)]$, where s_x and s_y are the sines of the angle along the x and y directions, then the first term is the unmodulated light from the hologram, the second term is the object wave, which has the necessary phase distribution, and the last term is the conjugate of the object wave with twice the linear phase of the reference wave. The hologram-recording process (carried out with a computer) and the optical reconstruction of the resulting phase distribution are shown in Fig. 10. The advantage of the HOE is that it is possible to generate the 3-D phase as close as possible to the design with both amplitude (efficiency $\simeq 10\%$) and phase versions of the element with a penalty on only the efficiency.[43] In this section, we describe some of the most used flat HOEs to generate OAM modes. Apart from these, volume holograms can also be used to generate OAM modes.[63–66]

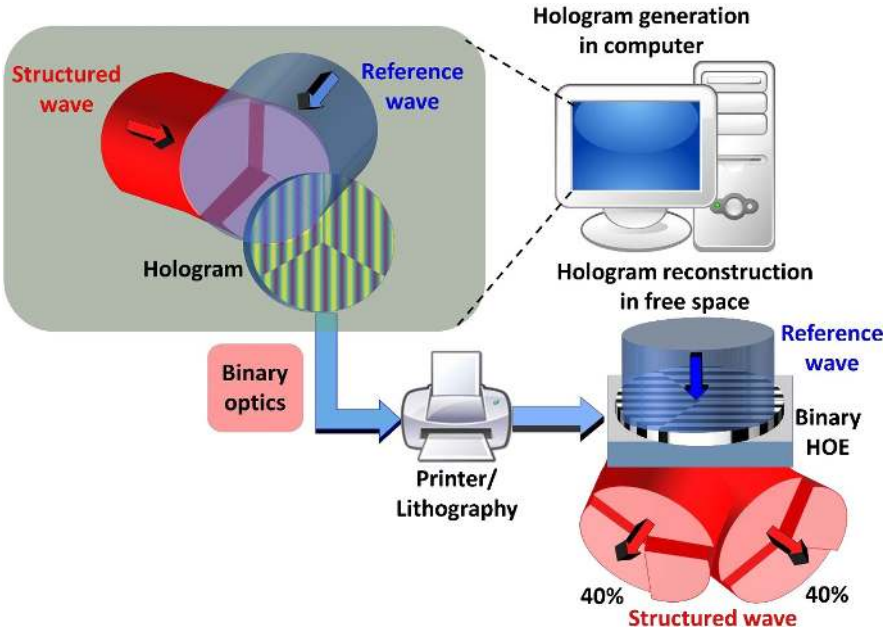

Fig. 10 Hologram recording within computer and reconstruction in free space.

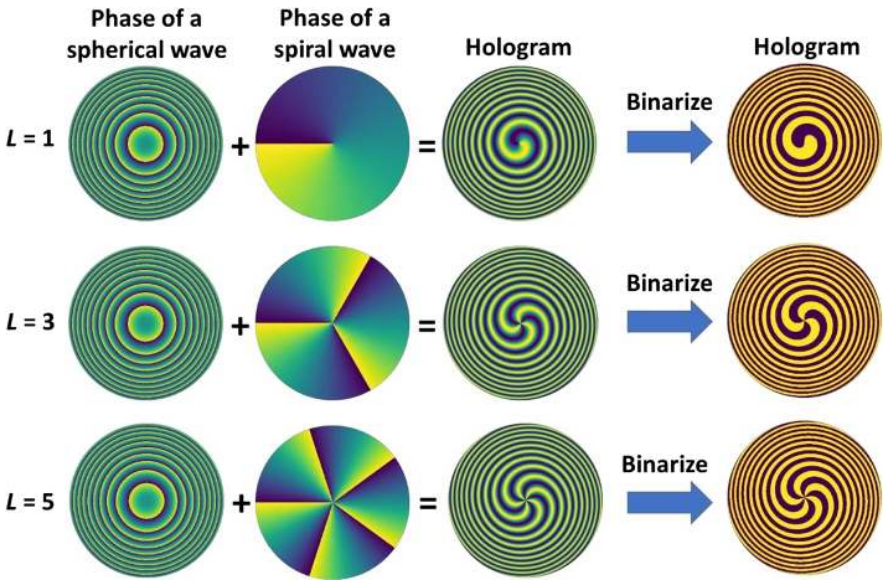

Fig. 11 Generation of holograms from interference between a spherical wave and spiral wave followed by binarization.

Spiral Fresnel zone plate. A spiral Fresnel zone plate is an HOE synthesized by the interference between a converging or diverging spherical wavefront with a spiral wavefront. The element can either be fabricated as an amplitude or a phase element, depending upon the efficiency requirement. It is necessary to convert the cosine modulation to a binary modulation in order to simplify fabrication.[43] The hologram formation can be mathematically expressed as follows: an electromagnetic wave with a complex amplitude $\Psi_1(x,y) = \exp[j(\pi/\lambda z)(x^2+y^2)]$ is interfered with a mutually coherent spiral wavefront with a complex amplitude $\Psi_2(x,y) = \exp[j\ell\theta]$, where ℓ is the topological charge that indicates the number of azimuthal 2π phase cycles. The phase image of the spherical wave and the spiral wave with topological charges ($\ell = 1$, $\ell = 3$, and $\ell = 5$) and the resulting interference patterns are shown in Fig. 11.

It can be understood from the above discussion that if the interference pattern $I = C_1 + C_2\exp[j\{(\pi/\lambda f)(x^2+y^2) - \ell\theta\}] + C_2\exp[-j\{(\pi/\lambda f)(x^2+y^2) + \ell\theta\}]$ is illuminated by a conjugate of the spherical wave, the spiral wave can be generated. On the other hand, if the interference pattern is illuminated by a plane wave with constant phase, then the spiral phase will be generated at the focal plane of the spherical wave. Let us extract one of the interference components, namely $\exp[-j\{(\pi/\lambda z)(x^2+y^2) - \ell\theta\}]$ (assuming $C_2 = 1$), which upon multiplication with the quadratic phase function $\exp[j(\pi/\lambda z)(x^2+y^2)]$ will result in $\mathfrak{F}[\exp(-j\ell\theta)]$ in the Fourier plane, where $\mathfrak{F}$ is the Fourier transform operator. Therefore, depending upon the incident wavefront, interesting behavior can be obtained in the output. Again, upon binarizing the hologram, the diffracted light consists of multiple complex fields corresponding to the Fourier components. Interestingly, the Fourier components of the spiral Fresnel zone plate occur along the optical axis, as shown in Fig. 12.[67,68] However, the efficiency of the various Fourier components are different depending upon the phase value of the binary levels.

Fork grating. A fork grating is an HOE generated by interference between a spiral wave and a tilted plane wave. The hologram formation can be mathematically described as follows: an electromagnetic plane wave with a complex amplitude $\Psi_1(x,y) = \exp[-j2\pi(\lambda)^{-1}(s_x x + s_y y)]$ is interfered with a mutually coherent spiral wavefront with a complex amplitude $\Psi_2(x,y) = \exp(j\ell\theta)$, and the binary holograms for $\ell = 1$ to 5 are shown in Figs. 13(a)–13(e), respectively. The holograms can be described as $I = C_1 + C_2\exp[j\{2\pi(\lambda)^{-1}(s_x x + s_y y) - \ell\theta\}] + C_2\exp[-j\{2\pi(\lambda)^{-1}(s_x x + s_y y) - \ell\theta\}]$. Upon illumination by a conjugate plane wavefront, a spiral phase wave is generated, and if illuminated by a plane wave, then the spiral phase

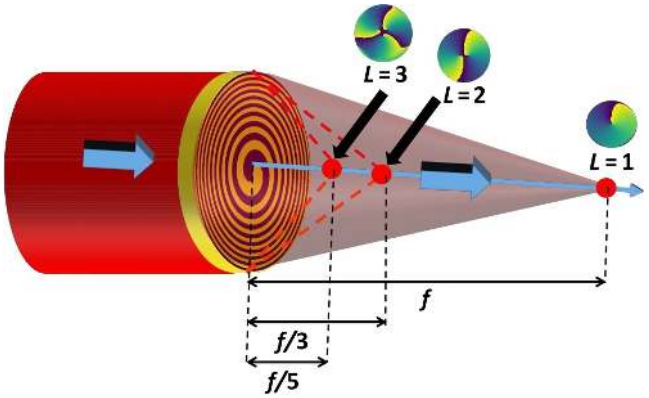

Fig. 12 Generation of spiral phases at different axial distances of a binary spiral Fresnel zone plate.

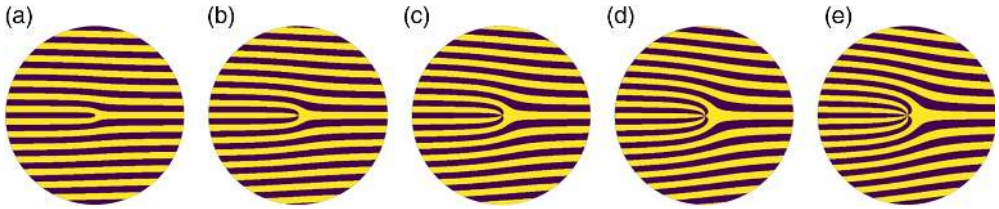

Fig. 13 Images of the binary fork holograms with topological charges: (a) $\ell = 1$, (b) $\ell = 2$, (c) $\ell = 3$, (d) $\ell = 4$, and (e) $\ell = 5$.

wavefront is diffracted away at an angle corresponding to the tilt of the original reference plane wave. When the fork grating is binarized and illuminated by a plane wave, the Fourier components of the grating are distributed over different lateral locations in the Fourier plane. The Fourier components with higher diffraction angles are associated with higher topological charges.[12,69–75] The diffraction of a plane wave by a binary fork grating is shown in Fig. 14. Therefore, it is possible to generate spiral wavefronts with different topological charges from the same element at the angles of the different diffraction orders. The orders will not have the same efficiency, however. The spiral Fresnel zone plate and fork grating are the most widely used HOEs for the generation of spiral wavefronts. Furthermore, both elements can be easily

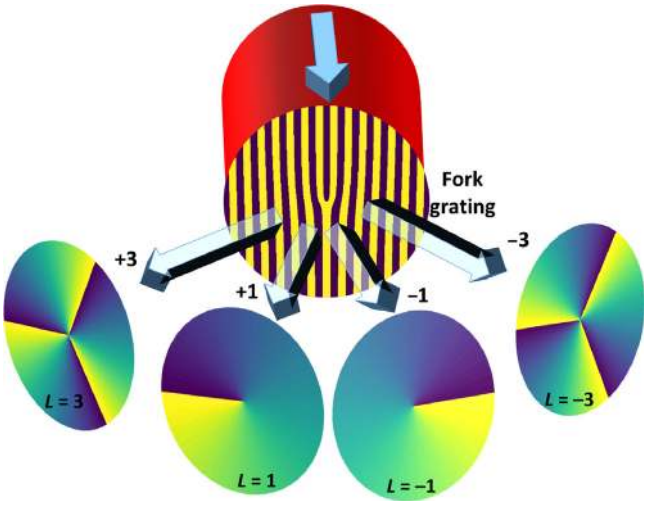

Fig. 14 Generation of spiral phase waves with increasing topological charges with increasing order of diffraction.

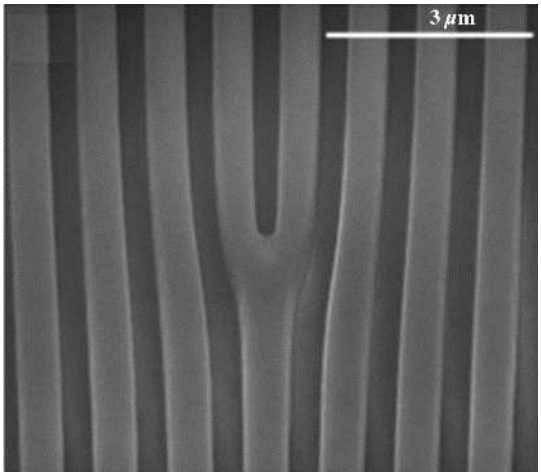

Fig. 15 Electron microscope image of a fork grating fabricated using focused beam milling (reprinted from Ref. 53).

fabricated using lithography techniques or printed on transparent sheets using inkjet printers.[76,77] An increase in the topological charge results in an increase in the number of lines in the fork in case of an HOE, whereas in the diffractive version of the SPP, the thickness increases. For this reason, the fabrication of an HOE is often easier for any value of the topological charge. In the case of OAM generation from fiber lasers, it is possible to fabricate the forked grating directly on the tip of fiber. This is very compact and avoids free-space coupling losses. An electron microscope image of a forked grating fabricated directly on the tip of an optical fiber is shown in Fig. 15.[53]

Trochoson. The name Trochoson is adapted from the Greek word "Trochos" meaning "ring" and is given to a spiral axicon, as first studied by Khonina et al.[78] The spiral axicon is a hologram obtained by interference between a spiral wave and a conical wave, as shown in the Fig. 16. The conical wave contains a distribution given as $\Psi_3(x,y)=\exp[-j(2\pi/\lambda)\alpha(x^2+y^2)^{1/2}]$, where α is the base angle of the cone. Later, the synthesis of a spiral axicon for the generation of

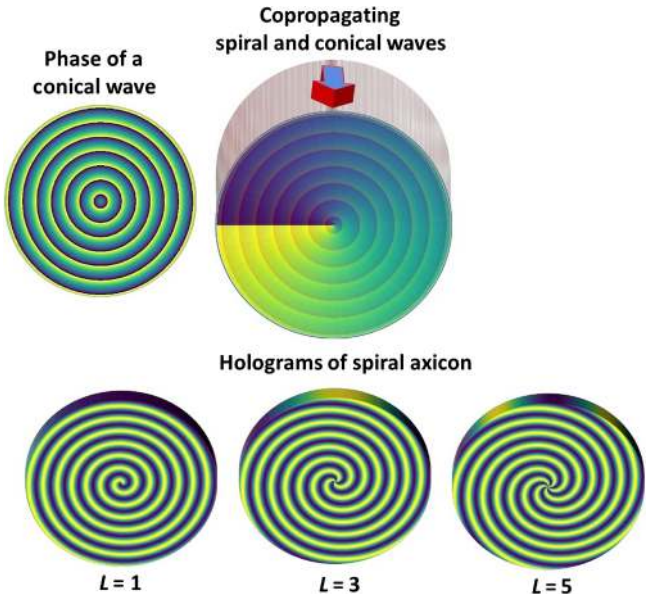

Fig. 16 Formation of spiral axicon hologram from interference between a spiral wave and a conical wave.

higher-order Bessel beams was reported.[79,80] As described earlier, it is possible to generate either a spiral wave or a spiral conical wave using different reconstruction beams.

Based on the above three examples, there were numerous reports on the generation of spiral beams carrying OAM using different types of carrier waves.[81–83] The choice of the carrier waves decides how the spiral beams are delivered in 3-D space. This same principle has been used to generate a variety of exotic complex light with OAM, such as Mathieu beams,[84] achromatic vortices,[85] modulated optical vortices,[86] optical-vortex filaments,[63] spiraling higher-order Bessel beams,[87] beams with fractional topological charges,[88,89] and perfect vortex beam.[90,91] The disadvantages of employing an HOE for the generation of special beams carrying OAM, such as lower efficiency, are discussed in Ref. 7 and the references therein.

Implementation using active devices. It should be noted that all the phase techniques and elements (such as the holographic technique and the forked grating) described in the previous section can be implemented using an active SLM such as LCoS.[74,92,93] The required holograms are calculated using the mathematical expressions described in earlier sections for generation of OAM modes. Let us consider the generation of OAM modes of azimuthal order (l) equal 1 to 6. The resulting phase patterns will be similar to those shown in Fig. 13. By illuminating the hologram with a reference Gaussian beam, the object is reconstructed and the OAM beams are generated at the far field, as shown in Fig. 17.

The azimuthal phase structure encoded with a sinusoidal grating provides the necessary phase structure to the diffracted orders. However, in this method, there is no control over the amplitude structure of the beam. For example, the OAM phase encoded in the sinusoidal gratings shown in Figs. 13(a)–13(e) generates additional intensity rings, which are not desirable. Scalar OAM modes with desired beam waist w, azimuthal order l, and radial order p, have both amplitude and phase structures. Such scalar modes can be generated using LCoS-phase-only SLMs by employing the algorithms proposed previously.[94–97] Among these, the Arrizón's algorithm is widely used because it has been demonstrated to provide relatively high SNR[98] and requires a phase range of only $<1.17\pi$.

In Arrizón's algorithm, any complex field $s(x, y)$ as expressed in Eq. (5) with amplitude function $a(x, y)$ ranging from 0 to 1 and phase function $\theta(x, y)$ can be generated using a CGH with the phase modulation function expressed in Eq. (6).

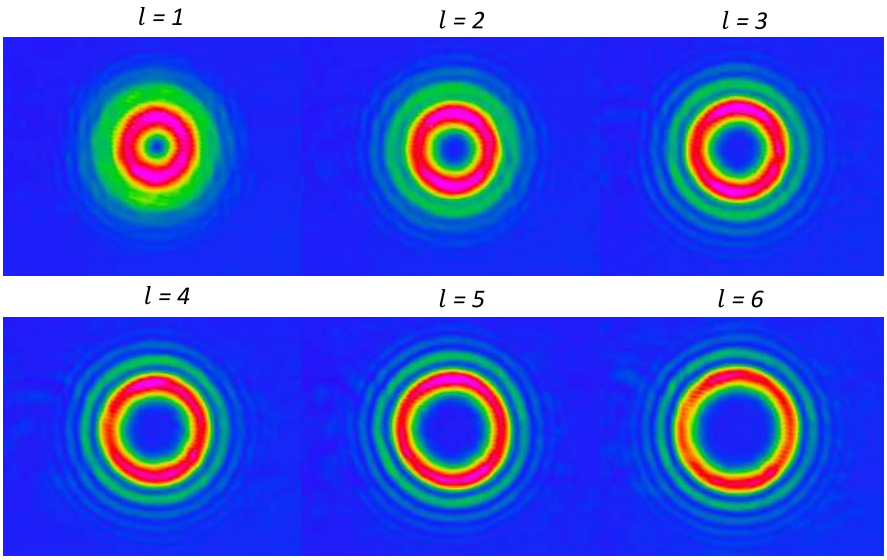

Fig. 17 OAM modes of azimuthal order *l* from 1 to 6 generated using the sinusoidal gratings programmed in the SLM.

$$s(x,y) = a(x,y)\exp[i\theta(x,y)], \tag{5}$$

$$\Psi(x,y) = f(a)\sin(\theta), \tag{6}$$

where $f(a)$ has to be accurately determined to generate the complex field, as explained below.

When a light beam with electric field U is incident on the LCoS device encoded with a phase modulation function, the beam is spatially modulated and the reflected beam from the device can be expressed in a Taylor–Fourier series expansion using the Jacobi–Anger identity[99] as

$$U\ \exp[\mathrm{if}(a)\sin(\theta)] = U\sum_{m=-\infty}^{\infty} J_m[f(a)]\exp(im\theta), \tag{7}$$

where J_m is the Bessel function of first kind with order m. In the Fourier series expansion, the phase of the first component ($m = 1$) is identical to the phase structure of the complex field. Hence, by equating the magnitude of the first component to the magnitude function of the complex field, as shown in Eq. (8), $f(a)$ can be determined:

$$f(a) = J_1^{-1}[Aa], \tag{8}$$

where A is a constant. The maximum value of A for which Eq. (8) will be satisfied is 0.5819. This corresponds to the first maximum of the first-order Bessel function J_1. Since the corresponding argument of the first-order Bessel function is 1.84, the required phase range of the SLM in this case is $-1.17\pi/2$ to $+1.17\pi/2$. Hence, by substituting Eq. (8) in Eq. (7), we generate a complex function $s(x,y)$ in the first harmonic of the above Fourier series. To achieve the spatial isolation of $s(x,y)$ from the other harmonics, a phase carrier $2\pi(u_0x + v_0y)$ is added to the phase of the encoded field θ [shown in Eq. (9)], where u_0 and v_0 are the spatial frequencies.[98]

$$U\ \exp\{\mathrm{if}(a)\sin[\theta + 2\pi(u_0x + v_0y)]\} = U\sum_{m=-\infty}^{\infty} J_m[f(a)]\exp[im\theta + 2\pi(u_0x + v_0y)]. \tag{9}$$

The resultant first-order diffraction from the SLM can be written, as shown in Eq. (10).

$$Ua(x,y)\exp[i\theta(x,y) + 2\pi(u_0x + v_0y)]. \tag{10}$$

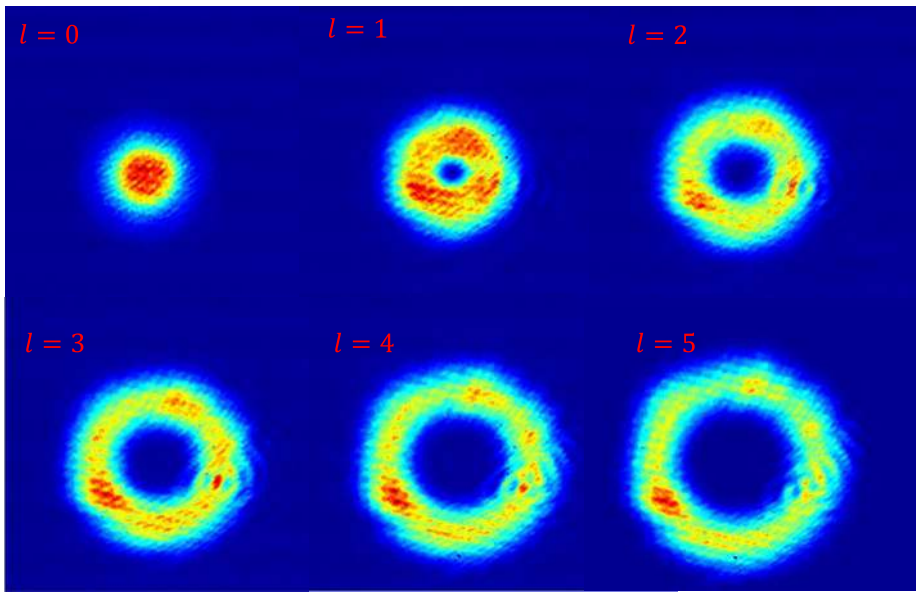

Fig. 18 Intensity profiles of zero-radial order OAM modes.

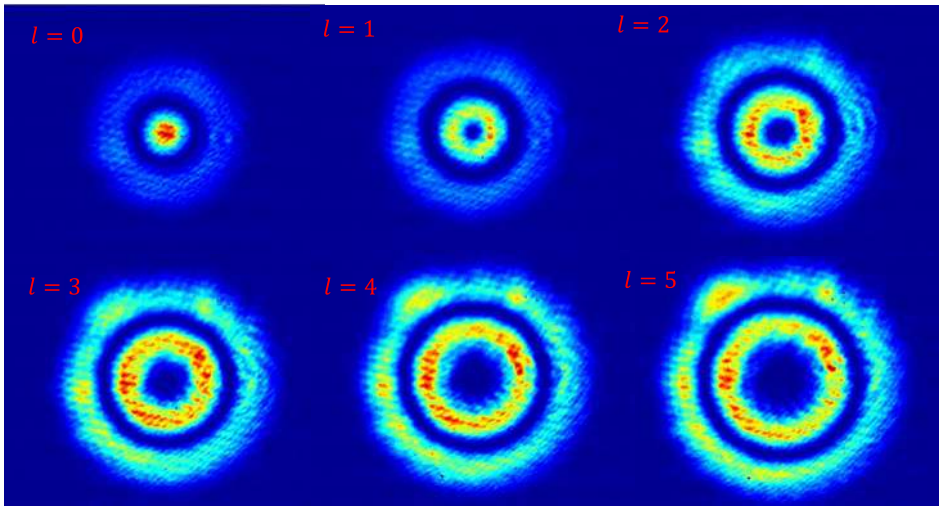

Fig. 19 Intensity profiles of first-radial order OAM modes.

By following this algorithm, CGHs for OAM modes of azimuthal order $l = 0$ to 5 and radial order $p = 0, 1$ were generated. The corresponding intensity patterns were recorded with a camera and are shown in Figs. 18 and 19, respectively.

Composite OAM modes, which are the co-axial superpositions of OAM modes, can also be generated using active LCoS SLMs.[100]

2.1.4 *Generation using all dielectric metasurfaces*

Optical metasurfaces[101,102] are artificial 2-D arrays of subwavelength meta-atoms that are designed to modify the amplitude, phase, and state-of-polarization of light. These devices are conceptually similar to the reflect-and-transmit antenna arrays,[103] which have been studied for decades in the microwave community. A typical meta-atom can have any shape that can support some form of resonance. When an electromagnetic wave passes through a patterned metastructure, the transmitted field amplitude and phase are modified according to the geometric parameters, such as height, length, and width, of the resonator. The transmission phase can be varied from 0 to 2π by changing one or more of these parameters. This results in the ability to fully manipulate optical wavefronts. The idea of using different structured surfaces to achieve spatially varying phase profiles has been used as early as 1993 in the microwave domain.[104] Early metasurfaces were, in fact, descendants of their microwave counterparts and were implemented using metallic meta-atoms. The major drawback of such metasurfaces is that they are made up of metallic structures, which are significantly lossy in the visible spectrum due to the strong absorption in metals.[105,106] However, these type of metasurfaces can be used in the infrared (IR) and higher wavelength spectrum as metals do not suffer from such losses at those wavelengths. Another popular method used in the design of metasurfaces is based on the Pancharatnam–Berry (geometric) phase. However, this method works only when the incident light is circularly polarized.[101] On the other hand, dielectrics exhibit very low losses at optical frequencies and support a magnetic resonance mode close to the electric resonance mode in the visible and IR regions of the spectrum. These facts have steered the direction of metasurfaces from metallic structures toward all-dielectric ones, whenever applicable. A more comprehensive study on material platforms for optical metasurfaces can be found in the paper by Choudhury et al.[107]

A typical meta-atom in a dielectric metasurface[108] is made up of a material with a high dielectric constant such as silicon or TiO_2. When excited with light, the meta-atom can support electric and magnetic dipole resonances. By varying one or more of the geometrical parameters of the resonator, one can spectrally overlap the electric and magnetic resonances at the wavelength of interest and obtain a 0 to 2π phase coverage.[109] Some widely used geometries for meta-atoms are V-shaped antennas,[110] cylindrical disks,[108] nanofin structures,[111] and cross shapes.[112] Other

shapes are also possible. Rational design thinking can be applied to come up with advanced geometries for meta-atoms. Different conventional optical elements such as lenses, gratings, beam splitters, and waveplates have already been successfully realized using metasurfaces. In some cases, a single metasurface has provided the functionality that may only be achieved by a combination of several conventional refractive optical elements.[113]

Another advantage of metasurfaces is that many of the techniques used to design the phase are similar to that of DOEs. In essence, they both impart spatially varying phase to the incident light. Identifying these key similarities is very useful for a metasurface designer. For example, the procedure involved in designing a Fresnel zone lens (FZL) phase profile is identical for both metasurfaces and DOEs. The only difference comes in the physical realization of the devices. DOEs use spatially varying heights of a dielectric (such as glass or lithography resist) to emulate the phase profile of the FZL, whereas the metasurface uses 2-D arrays of meta-atoms with spatially varying dimensions to accomplish the same. Usually DOEs have only two-phase levels making them less efficient. Their efficiency can be significantly improved by increasing the number of phase levels, which increases the complexity of the fabrication process. According to scalar diffraction theory, a phase profile with 16 levels can achieve almost 99% efficiency.[56] Either multistep lithography or grayscale electron beam lithography would have to be used and both of these processes can be difficult and hard to reproduce without error. However, a metasurface with multiple phase levels is relatively easy to fabricate. The reason being that metasurfaces produce spatially varying phase by changing the lateral dimensions of the meta-atoms. This means no multistep or grayscale lithography is required. Such metasurfaces can, therefore, create elements with much higher efficiencies than binary DOEs.

Design and fabrication of a metasurface with a specific phase profile. Designing a metasurface device can be divided into four main parts: (1) modeling meta-atom dimensions to achieve 0 to 2π phase coverage for the wavelength of interest, (2) generating the phase profile of the desired optical element, (3) converting the phase profile into metasurface GDSII layout, and (4) fabrication. Modeling the meta-atom starts with the choice of the meta-atom, e.g., cylinder and cross. After choosing an appropriate meta-atom, other geometric parameters of the meta-atom such as height, length, and lattice periodicity need to be optimized. This task is generally carried out using a commercial finite difference time domain (FDTD) solver such as Lumerical FDTD Solutions or CST FDTD Solver. Usually these geometric parameters are much smaller, compared to the operating wavelength. An initial rough simulation can be performed with approximate values for the geometric parameters of the meta-atom to obtain its transmission amplitude and phase. The next step in the design process is to vary one of the geometrical parameters over a range of values while keeping the remaining ones constant. The goal of this step is to obtain 0 to 2π phase coverage with uniformly high transmission amplitude across this entire range. This step can be thought to provide us with a lookup table containing the meta-atom dimensions for a desired transmission phase. It is the most challenging part of the simulation and this optimization usually requires several iterations to arrive at the final geometric parameters. It can typically take a few days to complete. Machine learning solutions are already making their way into solving this problem,[114,115] where models can predict the right geometrical parameters, given a desired operational wavelength. The second part in the design flow is the phase profile design, which has been discussed earlier.

The next step is to convert the phase profile from an image format into a metasurface layout in GDSII format. The phase profiles are usually generated as PNG, JPG or BMP files, where each pixel represents the transmission phase at that location. Each pixel can be considered to have a physical dimension when fabricated. On the other hand, in the metasurface layout, each pixel will be a meta-atom or a group of meta-atoms. Therefore, the phase images are converted into GDSII layout by a one-to-one mapping of the pixels in the phase profile to a GDSII layout, using the lookup table obtained from the FDTD simulations. It should be noted that each pixel in the layout is represented by a meta-atom that gives the desired transmission phase at that pixel location. An example layout for a spiral phase profile is shown in Fig. 20. Finally, this layout file is used to fabricate the metadevice using standard nanofabrication tools.

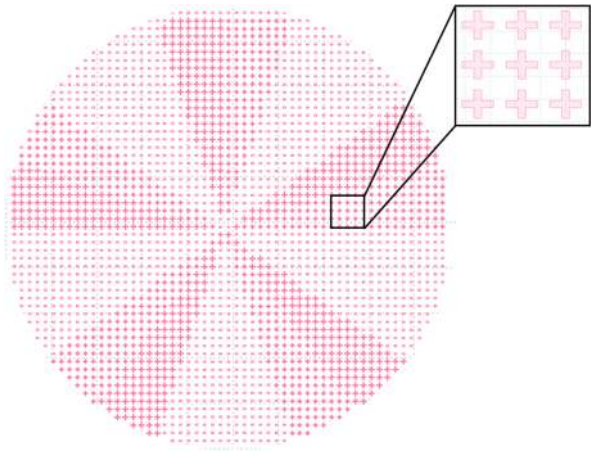

Fig. 20 GDSII layout of an SPP for generation vortex beam ($\ell = 5$) based on cylindrical-type meta-atom. The increase in the size of the cross gives a transmission phase of 0 to 2π.

Orbital angular momentum mode generation using metasurfaces. OAM generation in the IR region was first demonstrated by Genevet et al.[116] in 2012, using a V-shaped antenna-based metasurface SPP. In the next year, the same design concept was applied to the THz region to fabricate OAM generators.[117] Another modified version of the antenna was proposed to generate LG beams in THz domain.[118] Geometric phase metasurfaces that are composed of periodic arrays of birefringent subwavelength meta-atoms with spatially varying orientation have been used to generate both scalar[119] and vector[120] vortex beams. This type of metasurface works on the Pancharatnam–Berry phase phenomenon. Recently dielectric metasurfaces composed of Silicon nanofin structures have been used for polarization-sensitive generation and modulation of OAM beams.[121] A new concept of metasurface OAM holography has also been demonstrated.[122] This configuration is capable of reconstructing a range of distinct OAM-dependent holographic images from a single metasurface hologram. The metasurface was realized using gallium nitride (GaN) cylindrical pillars.

We have recently demonstrated a vortex beam generator[112,123] operating at 8.8 μm in the mid-IR spectral range using an all-dielectric metasurface composed of cross-shaped resonators. The meta-atoms can support both Mie-type electric and magnetic dipole resonances to realize spatial phase modulation and to completely suppress reflection losses. The schematic of the OAM generator is shown in Fig. 21(a). The length of the cross resonator is varied from 1 to 7.5 μm to achieve complete 0 to 2π transmission phase, as shown in Fig. 21(b). This figure is nothing but

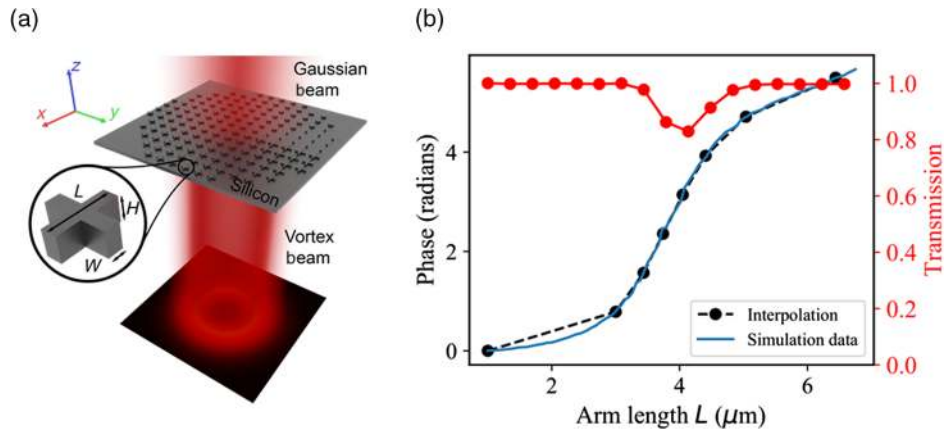

Fig. 21 (a) Schematic representation of the vortex generator layout, silicon cross meta-atom in the inset. (b) Lookup table for IR cross resonators: the length L of the cross arm is varied from 1 to 6.5 μm to achieve 0 to 2π transmission for IR design (reprinted from Ref. 112).

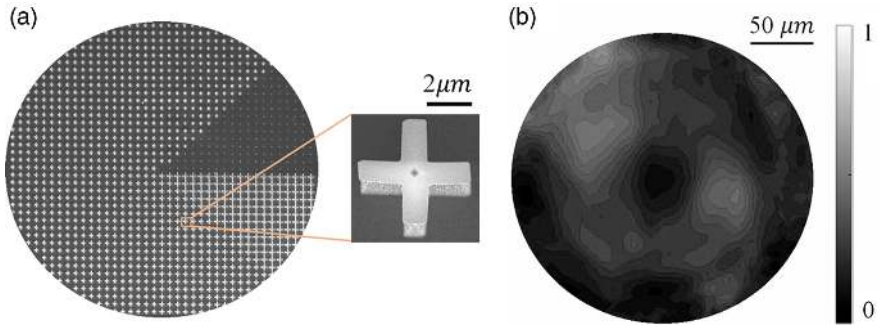

Fig. 22 (a) SEM image of meta-SPP for $l = +1$ topological charge; the inset shows the single building block. (b) Vortex beam image captured on the 64×64 pixel FPA detector (reprinted from Ref. 112).

the phase lookup table described earlier and can be used to construct the desired SPP element or any phase element. The scanning electron microscope (SEM) image of fabricated SPP and the experimentally captured vortex beam are shown in Figs. 22(a) and 22(b), respectively.

2.1.5 *Miscellaneous generation techniques*

Q-plate. A Q-plate is a liquid crystal (LC) device having an azimuthal pattern of the LC molecular director around a central point, as shown in Fig. 23,[125] and works based on the spin–orbit interaction (SOI) of light in anisotropic-inhomogeneous medium. The Q-plate pattern is characterized mainly by the topological charge q of the central singularity, which can be an integer or half-integer number. The Q-plates of topological charge q allow the generation of light beams carrying an OAM of $\pm 2q\hbar$ per photon, with the OAM sign controlled by the input polarization state. A Q-plate with $q = \pm 1/2$ transforming right circularly polarized beam into left circularly polarized beam with an azimuthal phase $\exp(i\phi)$ is shown in Fig. 23. Applying a suitable voltage across the device can reorient the LC molecules and hence modify the conversion condition leading to the generation of Hermite–Gaussian (HG) and LG beams, covering the whole "higher-order Poincaré sphere."

S-waveplate. This waveplate is a super-structured half-waveplate polarization converter created by femtosecond laser nanostructuring of glass.[126] It works on the principle of the SOI of light in a medium with form-birefringence. A beam of light without OAM but with right-circular polarization, when transmitted through the S-waveplate, changes to a left circular polarized beam with OAM, as shown in Fig. 24. While this generation method results in optical beams with fixed OAM, its main advantage is that it can be used for high-power and high-energy laser applications, in which other devices would be damaged.

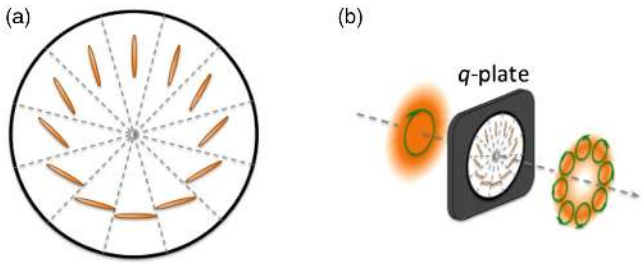

Fig. 23 (a) Structure of the segmented $q = 1/2$ plate, with indication of the LC director orientation. (b) Q-plate transforms right circularly polarized beam into left circularly polarized beam with an azimuthal phase $\exp(i\phi)$ (reprinted from Ref. 124).

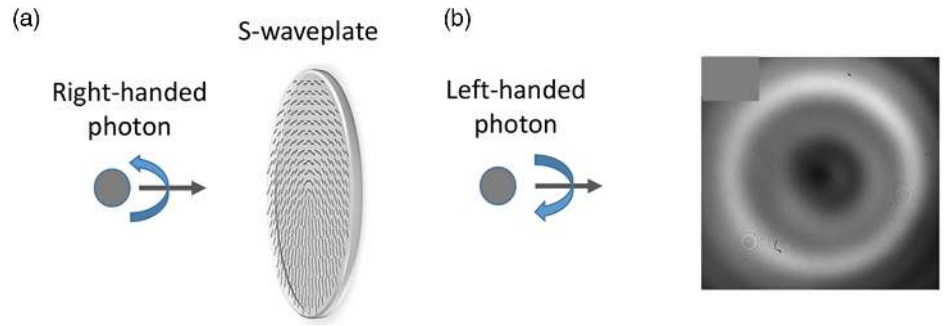

Fig. 24 (a) Light with right circularly polarization and no OAM transmitted through the S-waveplate changes to left circularly polarized OAM beam. (b) Measured intensity profiles of left circularly polarized OAM beam (reprinted from Ref. 21 with the permission of AIP Publishing).

2.2 *Amplitude Modulation Approach*

In the previous section, we discussed the generation of OAM modes using a phase modulation approach. Similarly, we can potentially generate OAM modes using an amplitude modulation approach as well. For example, OAM mode generation is possible using a DMD. A DMD consists of a 2-D array of pixels, which can only be turned ON or OFF. It is capable of projecting both binary and grayscale images at high frame rates. Phase patterns cannot be generated directly using a DMD. Therefore, the most common methods of generating such patterns use phase-only SLMs or fabricated DOEs. Special techniques have been developed by which a DMD can be used to create phase patterns.[127,128]

In this section, we look at methods that generate complex amplitude patterns using binary amplitude modulation through the mirrors of a DMD. Several techniques based on holographic approaches have been explored in Sec. 2.1.3 of this paper. These principles are applied in the techniques used when DMDs are employed for generation of phase patterns. The slight modifications that need to be made as the DMD is a binary amplitude device are discussed in this section. For example, Brown and Lohmann[60,129] demonstrated binary holography and Lohmann and Paris[130] demonstrated binary computer-generated Fraunhofer holograms. While the paper was published in a pre-DMD era, the technique is of particular interest as they used binary amplitude-only holograms and produced desired phase patterns. This was achieved using a technique known as the "detour phase" technique. A seminal review on CGHs done by Tricoles[62] discussed not only these holographic techniques but also their importance in applications such as medical diagnostics, imaging, data processing, and high energy physics. It should be noted that the desired patterns are generated in the far field of the holograms, using these techniques.

In a study published by Piestun et al.,[131] on-axis CGHs were used to modulate phase in the Fresnel plane, using a Fresnel transform and progressive binarization. In 2010, Ren et al.[132] succeeded in generating LG beams using a DMD. In this case, the DMD was loaded with computer-generated fork-like patterns of different topological charges. The patterns were first corrected for intensity because the gamma curve of the DMD is not linear. Goorden et al.[133] reported the superpixel method in 2014. We look at three of the most commonly used techniques for phase generation using a DMD. An LG beam of charge 1 is used as a test intensity and phase pattern to compare the various methods. It should be noted that the DMD can only generate the desired phase pattern if it is placed in the relevant experimental setup.

2.2.1 *Superpixel method*

In this method, square matrices of pixels were combined into superpixels. By controlling the index and number of the pixels in a superpixel that are turned ON, the required amplitude and phase values can be achieved. The experiment is set up such that each individual pixel in a superpixel possesses a phase prefactor. The field at all points can be represented in phasor form using this approach. The method requires a typical $4f$ system, as seen in Fig. 25(a). The DMD (with required pattern) lies in the input plane. A spatial filter in the back focal plane filters out

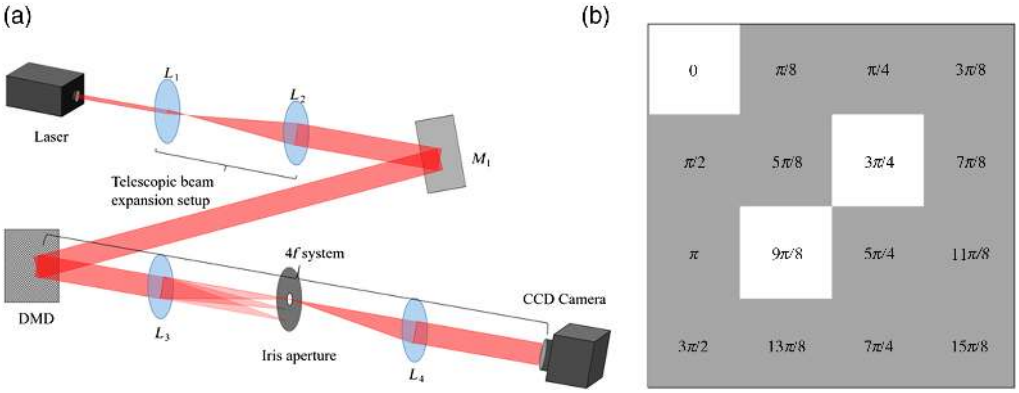

Fig. 25 Superpixel method: (a) setup for superpixel method and (b) superpixel with phase prefactors.

a particular order, which will form the image in the output plane.[133] The pattern on the DMD consists of several superpixels, with each superpixel representing the intensity and phase of one point at the output plane. In an $n \times n$ superpixel, each individual pixel contains a phase prefactor, as a result of the optics following it [see Fig. 25(b)].

The field at any point on the output plane can be represented as a vector sum considering each ON pixel as a vector of intensity $1/16$ and phase as the complex angle. Turning certain pixels ON will give a resultant field $E_{\text{superpixel}}$, whose intensity and phase will depend, respectively, on how many and which pixels are ON.

The aperture in the back focal plane in the $4f$ system plays a major role in this method. Its position is calculated such that the pixels within each superpixel contain specific phase prefactors. For an $n \times n$ superpixel, the location of the aperture is given as $(x, y) = (\pm a, \pm na)$, where $a = \lambda f/n^2 d$. Here λ is the wavelength of light used, f is the focal length of the first lens in the $4f$ system, and d is the pixel dimension [micromirror pitch of the DMD (Texas Instruments 6500 evaluation module), $\sim 7.6\ \mu$m].

A way by which to use this method is described. Initially, the value of n is chosen, say $n = 4$. Then, we generate a lookup table that contains all 6561 possible vectors and the pixel combinations for them. The correct combination is pulled out of the table for each desired value of the field at each point in the target plane. We use these calculations to generate a 400×400 pixel LG_{10} beam. One limitation is the trade-off between the size of the desired field and resolution.

Figure 26(a) shows the DMD pattern generated using the superpixel method for LG_{10} beam. We conducted an experiment to verify and obtained the output shown in Fig. 26(b). The first image is that of an 400×400 pixel LG beam interfered with a reference beam. The second image is a zoomed-in version of the same interference pattern near the phase singularity. We can clearly see the fork pattern, confirming the spiral phase.

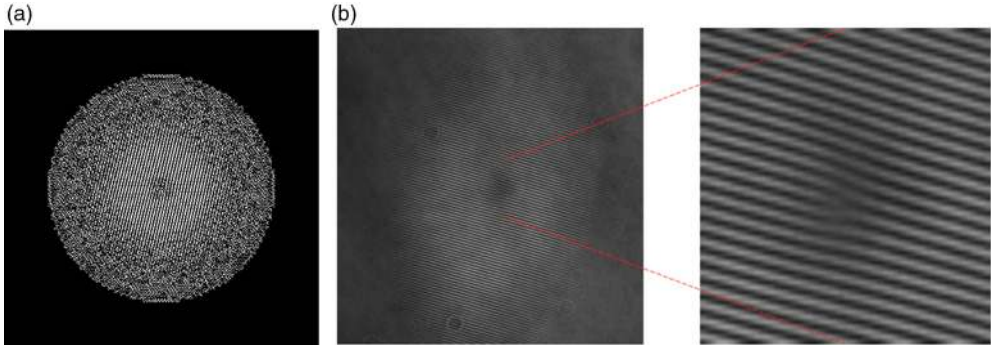

Fig. 26 Superpixel pattern and output: (a) pattern generated for LG1 beam and (b) interference of LG1 beam generated using the superpixel method and a Gaussian beam.

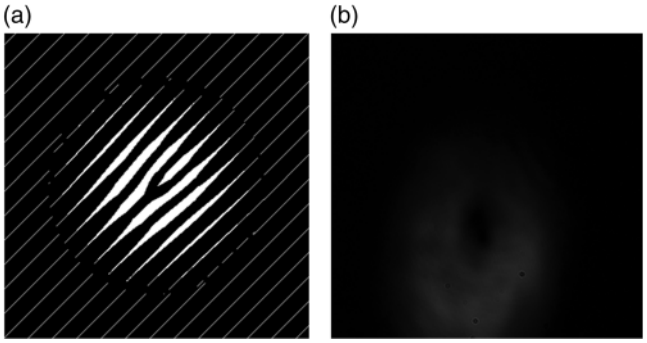

Fig. 27 Lee pattern and output for a 400×400 pixel LG1 beam: (a) pattern generated using Lee holography and (b) experimental output of Lee holography.

2.2.2 *Lee method*

This is essentially a holographic technique, where the hologram is generated using the desired pattern, and it is binarized on the basis of the intensity and phase at each point.[134,135] The setup is similar to that of the superpixel method, i.e., a $4f$ setup with an aperture in the Fourier plane to select a particular order of interest. The equation used to generate the binary hologram is given below. The binary hologram thus generated is shown in Fig. 27(a).

$$h(x,y) = \frac{\mathrm{mod}_{2\pi}[\phi(x,y) + 2\pi(kx + ky)] - \pi}{2\pi} <= \frac{\sin^{-1}\{abs[E(x,y)]\}}{\frac{\pi}{2}}. \tag{11}$$

In this equation, $h(x,y)$ is the binary value of each point on the DMD pattern; $E(x,y)$ and $\phi(x,y)$ are the normalized amplitude and phase at each point in the desired pattern, respectively; k is the carrier frequency that determines both the fringe width of the pattern and the separation of the different orders in the Fourier plane. The mod or modulo operation of the phase term with respect to 2π gives the remainder of the phase term when divided by 2π, or, in other words, we wrap the phase. Hence, we subtract π from it to make the average value 0.

All these techniques are very susceptible to alignment of both the pinhole and the DMD. This is clear as seen by the experimentally generated LG_{10} beam using this method shown in Fig. 27(b). The nonuniformity of intensity along the azimuthal direction is an artifact of the misalignment stemming from the aperture positioning and the way the DMD is held.

2.2.3 *Binary Fraunhofer holography*

This method is best explained by referring to a simple explanation of binary diffraction gratings. Two rays leaving two adjacent grating slits and going into the first diffraction order at the far field have a path difference of one wavelength.[60] Their detour phase is 2π. However, if a slit is slightly out of position, the emerging wavefront will diffract differently, thereby creating a different intensity and phase pattern in the far field. It is this principle of detour phase that is used to generate any phase pattern.[130]

In Fig. 28(a), $u(x,y)$ is the desired LG_{10} pattern, which will be obtained by the Fourier transform of $U(\nu_x, \nu_y)$. This expression is encoded as a hologram by interfering the pattern with a reference wave. The resultant pattern is binarized $H(\nu_x, \nu_y)$ and this is what is loaded on the DMD or holographic plane. To simulate a 2-D grating, whose slits are adjustable, the DMD is divided into groups of pixels that we call cells. While this may seem similar to the superpixel or Goorden technique, it should be noted that those techniques are $4f$ methods, whereas the binary Fraunhofer technique is a $2f$ one. A cell in the holographic plane represents each element in $U(\nu_x, \nu_y)$. And in turn, each element in $U(\nu_x, \nu_y)$ will be represented by say $n \times n$ pixels. Figure 28(b) is a representation of a cell. As with the Goorden technique, there is a clear trade-off between the number of pixels within a cell and the overall resolution with which a pattern can be generated.

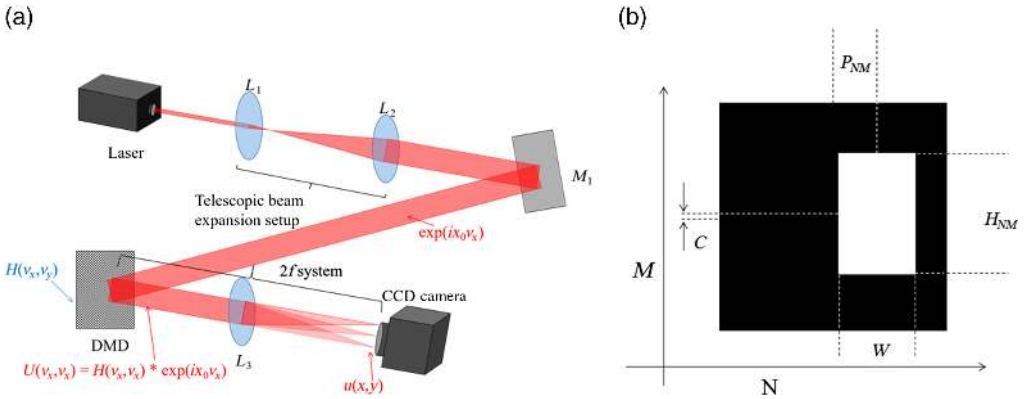

Fig. 28 Binary Fraunhofer holography method: (a) schematic representation of binary Fraunhofer holography method and (b) cell.

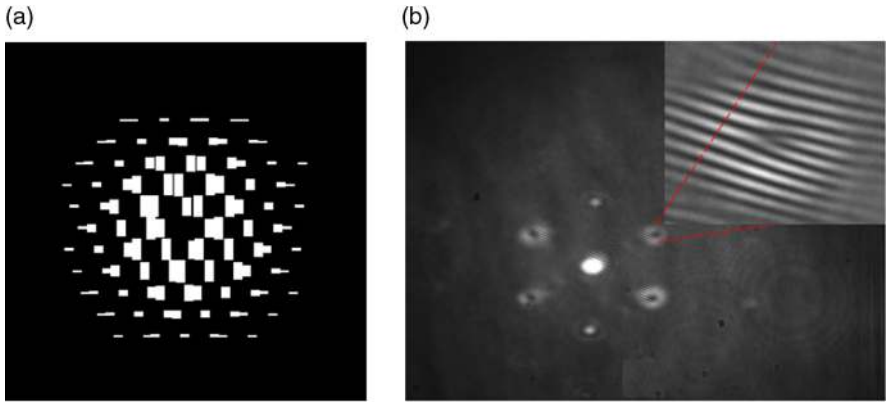

Fig. 29 Experimental output of binary Fraunhofer holography: (a) pattern for LG1 beam and (b) interference of LG_{10} beam and a reference beam.

Figure 29(a) shows the pattern generated for an LG_{10} beam using the binary Fraunhofer holography method, and Fig. 29(b) shows the output in the Fourier plane. The zeroth order is bright and contains no phase information, just like a regular hologram. A zoomed version of the interference pattern obtained with one of the orders is shown as an inset. The fork pattern shows that the beam generated contains a spiral phase.

Three techniques for using an amplitude element such as a DMD to generate complex amplitude patterns have been discussed. All these methods typically have a poor efficiency compared to direct phase modulation achieved using an active LCoS device. However, the DMD offers much faster switching, and the device itself is much cheaper than the LCoS device. Of the three techniques described above, the Lee method is most commonly used. However, the binary Fraunhofer method is simpler to set up due to the fact that it is a $2f$ method.

2.3 *Hybrid Approach*

So far, a variety of active and passive approaches for generating OAM modes have been discussed, including diffractive elements, holographic elements, and DMDs. The serious drawback of all the methods described so far is that the OAM mode is generated in free space and is not amenable for coupling into an optical fiber. In this section, we discuss an all-fiber technique for the excitation of an OAM mode using a fused fiber coupler. Such an approach would be quite valuable for applications such as optical fiber communication.

The fused-coupler approach is based on selective coupling between different modes in two dissimilar fibers. Previously, such a technique has been used to achieve coupling between the

fundamental HE_{11} mode in an SMF and a selected higher-order LP mode group in a few-mode fiber (FMF).[136] However, the selective excitation of OAM modes within a mode group in typical step-index FMFs cannot be achieved using such couplers. This is due to the fact that the targeted modes in the FMF nearly degenerate with other OAM modes of the same $|l|$ ($l > 1$) consisting of even/odd HE or EH eigenmodes, or, in the case of $l = 1$, with the transverse electric (TE_{01})/transverse magnetic modes (TM_{01}) modes. Since breaking such degeneracy in FMFs is essential for the excitation as well as stable propagation of the OAM modes,[137] a solid core fiber may be used. The solid core fiber breaks the degeneracy between the desired HE_{21} modes and neighboring TE_{01} or TM_{01} modes, thereby allowing the preservation of the excited OAM mode without significant intermodal coupling.[137] Phase matching between the HE_{11} mode in the SMF and the desired mode in the solid core fiber can be achieved by pretapering the SMF and then fusing both fibers.[136] As such, it provides a promising alternative pathway to directly couple the traditional Gaussian beam to the desired OAM modes with high purity and good stability in an entirely integrated scheme. In addition, this all-fiber device could potentially generate OAM modes with higher charge as the above phase-matching technique could be extended to other OAM modes supported by the solid core fiber[138]

Based on simulations, the fused coupler described above is fabricated using the modified flame-brushing technique.[139] A schematic of the experimental setup used for characterization of the fabricated fused coupler is shown in Fig. 30. Light from a 1550-nm laser source (spectral width ≈0.08 nm) is split into two arms using a commercial 3-dB coupler. Light from one arm of the 3-dB coupler is used as a reference for the interference setup to analyze the OAM beam at the output of the fused coupler. The output beam from the solid core fiber is collimated with a lens ($f = 6$ mm) and imaged using a CCD camera (MicronViewer-7290A). The output beam from the reference SMF and solid core fiber (cleaved at ≈40 cm beyond the interaction region of coupler) are combined using a free-space beam splitter to form the interference pattern. The interference setup (shown in the dotted box) is used to determine the charge ±1 of the generated OAM mode by observing its characteristic fork and spiral patterns.

The above fused fiber coupler technique has been extended by different groups for exciting the OAM modes in fibers with different index profiles and also in photonic lanterns. Heng et al.[140] reported the generation of an OAM mode of charge 1 in a graded index FMF with a mode purity of 95% over 100 nm (1500 to 1600 nm) bandwidth. Wen et al.[141] reported amplification of OAM modes generated using fused couplers, which have an 160-nm bandwidth (1480 to 1640 nm). This technique was further scaled for exciting the higher-order circularly polarized OAM modes ($l = \pm 2$) using a ring core fiber,[142] and a modal power extinction ratio of 12.9 dB was reported with respect to the neighboring modes. The fused coupler technique is employed in making mode-selective photonic lanterns (MSPLs) exciting five OAM modes in a ring core fiber with a bandwidth of 500 nm (1000 to 1500 nm).[143] More recently, Li et al.[144] have reported on the simulation of MSPL for three OAM modes with a modal cross talk of less than −24 dB. Such results help in highlighting the immense potential of the mode-selective fused fiber coupler approach for the generation of desired OAM modes.

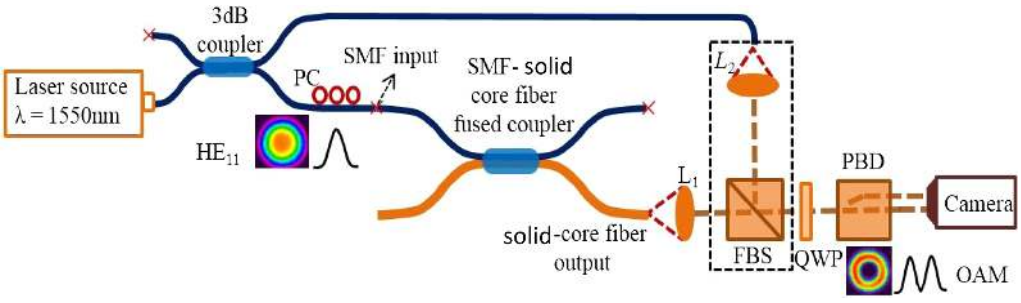

Fig. 30 Experimental setup for characterizing the generated OAM beam: solid lines are propagation path of light through the fiber; dashed lines are that of light through free space. PC, polarization controller; L1 and L2, collimating lens; FBS, free space beam splitter; QWP, quarter waveplate; and PBD, polarization beam displacer.

2.4 *Generation of Optical Vector Beams*

The fact that the state of polarization (SoP) across an optical beam need not be uniform at different spatial locations at the same time or at different times led to the realization of vector optical beam (VOB). VOBs are a class of solutions to the vector wave equation in the paraxial limit. These solutions along with axial symmetry around the beam axis are known as cylindrical vector beams (CVBs). Radial and azimuthal polarization can be considered as special cases of CVBs. The spatial inhomogeneity of the SoP of the optical beams can be cylindrically symmetric or asymmetric, leading to unconventional polarization states depending on the generation method. An authoritative review of this area of research presented previously [145–148] provides details from fundamental aspects to emerging applications. The exploration of CVB capabilities is still largely limited to optical physicists and has recently been used as a tool to access electromagnetic properties of matter, including a novel way of studying and controlling edge currents in topological materials and for Floquet engineering of nonequilibrium states of matter.[149]

In addition to the spatial variation in the SoP, it is possible to modify the phase front of the optical beam either independently or together. In the first situation, the wavefront can be made helical or in some alternate shape determined by a polynomial or special mathematical functional form. For example, this could be used to generate optical beams with vortices or beams that are Airy, HG or some other exotic form with unique phase structure. Such demonstrations have proved to be useful for several obvious and unforeseen applications in the classical and quantum domains. The following discussion provides a detailed, current status account of the generation, detection, and manipulation of optical vortex beams (OVB) with an OAM DoF.

Ensuring that the SoP and the phase DoFs of an optical beam are nonseparable results in beams that embed both characteristics. Such beams are known as "vector-vortex" beam (VVB),[150,151] polarization singular (PS) beams,[152,153] Poincaré beam (PB),[154] spin–orbit beams,[155] or classically entangled beams.[156] In all these paraxial optical beams, the SoP shows spatial variation due to the underlying variations in the phase structure. Under special circumstances, the spatial variation can also lead to the appearance of geometric phase due to variations in the SoP and can be understood as arising due to optical SOI.[157] SOI refers to the nonseparably coupled spin and OAM of a paraxial light beam. Mapping the phase-polarization structure on the Poincaré sphere, these beams are also known as PBs, a 2-D projection of the Poincaré sphere on any given plane. For example, a projection of the top half of the Poincaré sphere onto the (S_1–S_2) Stokes parameter plane leads to a beam, whose SoP in the beam cross section varies radially outward with different ellipticities from the axial (S_3) point. Such a construct leads to the appearance of "C-point" and "L-line" polarization singularities, corresponding, respectively, to a point where the orientation of the polarization ellipse is undetermined and a symmetric ring around which the spin direction is undetermined. The C-point corresponds to purely circular polarization state ($S_3 = 1$), also known as polarization vortex, and the L-line is where the SoP is linear ($S_3 = 0$). The appearance of C-point and L-line polarization singularities and spatially varying (vector) SoP gives the optical beams the appropriate names mentioned.

The lowest-order polarization singularities and the associated topological structure in the ellipse field typically classified as lemon, star, and monstar[158,159] are shown in Figs. 31(a)–31(f) along with the first higher-order spiral, node, and saddle structures. They are characterized by their index $I_c = \pm 1/2, \pm 1$, denoting the rotation of the disinclination around the C-point. Extending beyond the half-turn around the C-point, higher-order disclination indices $(I_c = \pm 2, 3)$ have also been investigated and were recently experimentally demonstrated. Such optical beams are represented in higher-order spherical space, also known as the C-point sphere.[160,161]

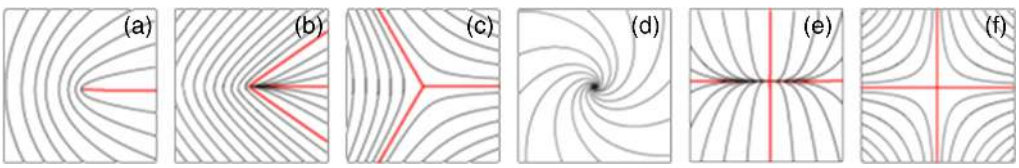

Fig. 31 Topological structures associated with singular points: (a) lemon, (b) monstar, and (c) star of index $\pm 1/2$ and (d) spiral, (e) node, and (f) saddle of index ± 1.

The C-point singularity and the surrounding elliptical-linear SoP in the beam cross section are formed by superposing a helical-phase optical vortex (LG) beam and a plane wave Gaussian beam in two orthogonal circular SoPs.[162] Alternatively, they may be formed via superposition of two LG beams in orthogonal circular SoP.[161] Mathematically, they are represented as[161,162]

$$\Psi(r,\phi) = f(r)[(\cos\beta e^{il_1\phi} + \sin\beta e^{i-l_1\phi e^{i\gamma}})\hat{e}_R + e^{il_2\phi}e^{i\delta}\hat{e}_L], \tag{12}$$

where β, γ, and δ are phases; r and ϕ are the polar coordinates in the plane perpendicular to the propagation direction; l_1 and l_2 are the topological charges of the spatial modes with radial variation $f(r)$, and $\hat{e}_R$ and $\hat{e}_L$ are the unit vectors of right- and left-circular SoPs, respectively. The topological charges of the beam l_1 and l_2 can take any arbitrary integer or noninteger value to obtain different patterns, and with $l_2 = 0$ we obtain the lowest-order PS pattern with $I_c = \pm 1/2$. These topological phase-polarization structures can be used to engineer the total Poynting vector density arising due to the combination of the SAM and the OAM. One can expect many exciting possibilities for new fundamental studies and applications, based on these concepts.

2.4.1 *Generation methods*

As described above, one of the characteristic features of vector wave fields is the appearance of C-point and L-line polarization singularities and disclinations[163–166] in the transverse cross section due to on-axis or off-axis superposition of two or more wave fields with different phase-polarization structures. In a field of elliptical polarization, C-point singularities are locations where the elliptical SoP degenerates to circular SoP, wherein the azimuth of the circular SoP is undefined. On the other hand, the L-line singularities correspond to locations where the polarization ellipse degenerates to linear SoP with undefined ellipse handedness. It is important to note that the C-point and L-line singularities are fundamental features of vector wave fields, where the SoP of the beam field is spatially inhomogeneous and elliptically polarized. These are an important source of information to explore a variety of fundamental aspects of light, light–matter interaction, and their applications.[166,167] These unique signature field patterns were first observed in the microwave region[168–170] and were subsequently measured and studied in several optical systems, including in speckle fields, in polychromatic fields, and in scattered radiation.[167] The speckle beam fields with a large number of randomly oriented polarization singularities are generated by propagation of polarized light through an inhomogeneous and weakly birefringent medium such as a multimode optical fiber. This results in an elliptically polarized field in the output rich in polarization singularities.[171] Such elliptically polarized light fields with myriad of randomly located PS C-points and L-lines act as markers in a number of applications, including characterization of rough surfaces and biological tissues.[167]

A well-defined optical beam field containing an elementary polarization cell embedded with one C-point bounded by an L-contour has also been demonstrated and applications using such beams are emerging. The polarization singularity features in a beam are associated with the optical AM of beam fields and appear due to the simultaneous presence of both the spin and OAM DoF in a beam. Optical beams with components of both SAM ($\pm\sigma = 0, 1$) and OAM ($\pm l = 0, 1, 2$) attributes present simultaneously, contribute to the total angular momentum (TAM) ($\pm\sigma l$) of the beam. Such beams have been generated using different methods and technology platforms.[150–157] Known initially as VVBs, the optical singularities are formed around a point where a scalar vortex is centered in at least one of the scalar components of the vector wave field. Propagating a polarized light beam through a two-mode optical fiber (TMF) instead of a multimode optical fiber generates a well-defined and controllable optical beam containing an elementary polarization cell embedded with one C-point bounded by L-contour.[152] Such beams are formed due to the linear superposition of a collinearly propagating vortex mode and the fundamental mode in the optical fiber. Such beams have also been generated using geometric phase elements, such as subwavelength gratings,[172,173] wherein the Pancharatnam phase was shown to play a critical role in the AM of the beam.[174] The role played by the geometric phase in such beams is indicated by its evolution during propagation, which indicates that VVBs carry OAM. This led to the realization that VVBs can also be identified by the presence or absence of

TAM carried by the beam, and geometric phase has been shown to play a critical role in this beam attribute. In addition to TMFs,[150–153,162] VVBs have also been generated using a variety of methods, including interferometry,[145–147,175] LC Q-plates,[125,176] optical crystals,[177–179] stressed optical element,[154,180] and, more recently, using structured metasurfaces[181–183] and in plasmonic-fields.[184]

Generation of the family of VVBs using LCoS devices[74,185–187] and their recent off-shoot the DMDs[132,188] were notably missed in the above discussion as they belong to active and flexible generation methods. DMDs are finding more and more uses in research labs for the generation of a wide variety of complex beams. They are cheaper and faster than LCos devices. Though LCoS devices are considered expensive compared to other optical elements used in this area of research, the flexibility they bring to generating a large variety of phase-polarization structured optical beam far outweigh the cost. Moreover, they have almost become a staple in all optics-photonics research laboratories involved in the above research activity, which is rapidly pushing the cost down. Having been around for more than a decade now, a number of research articles have been reported on the use of LCoS SLMs to generate vortex beams, vector beams, VVBs, and a large number of phase-polarization-intensity-modulated complex light beams with custom purpose. Most of these are reviewed authoritatively in the references.[74,185–187] More interestingly, the spatially inhomogeneous polarization and helical-phase wavefront can coexist in the same light beam and thus form cylindrical VVBs or PBs of different orders.[189] Its perfect version[190] generated using SLMs provides additional DoFs with a large variety of patterns and offers an almost unlimited experimental flexibility for beam and thereby material manipulation. In addition to manipulation of the phase-polarization pattern of the light beam, the underlying geometric phase aspect of the beam has also been modified to generate PBs.[191] Needless to emphasize, several alternate methods are being actively pursued as well.

Based on the formalism given in the introduction part of this section, we have generated the lowest order and the first few higher-order VVBs using a superposition of vortex (LG) beams and a Gaussian beam with suitable spin and orbital AM (Figs. 32 and 33). The Poynting vector density and the total AM[192] of such beams are quite complex in the cross-section. In addition to integer charges, we were able to generate fractional charge VVBs, which could find potential application elsewhere. Decomposition of the beams into their fundamental constituents is typically carried out via interferometry, polarimetry,[150–153,192] or vector decomposition using LCoS SLMs.[74,185–187]

A brief overview of the current status of vector-vortex optical beams generated with contributions from both spin and OAM DoFs has been presented in this section. The lower, higher, and fractional order VVB results presented here are generated using LCoS SLMs. In all cases, the appropriate circular polarization of the input beam and phase mask are projected on the LCoS SLM to generate the vector beam. The spatial polarization characteristics of the beams are obtained using imaging Stokes parameter measurements. Such phase-polarization structured optical beams are beginning to find applications in optical microscopy, communication, and material characterization.

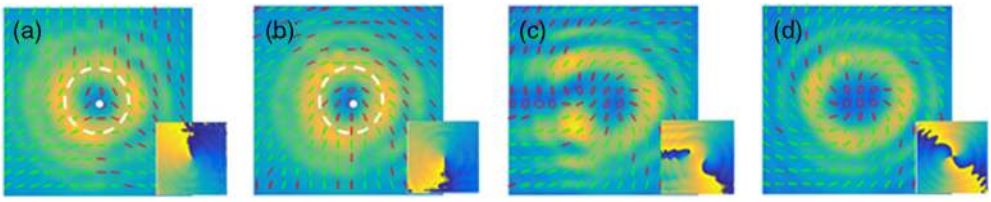

Fig. 32 PS beams generated using LCoS SLM and measured using polarimetry. Topological pattern of (a) star, (b) lemon, (c) fractional charge, and (d) node. The SoP of the beams measured (red and green colors) are plotted overlaying the beam intensity (yellow color); white color dots are the C-points and white color dotted rings are the L-line in the beam cross section. Inset shows the phase map of the beams highlighting helical phase structure, with yellow and blue colors corresponding to 0 and π phases, respectively.

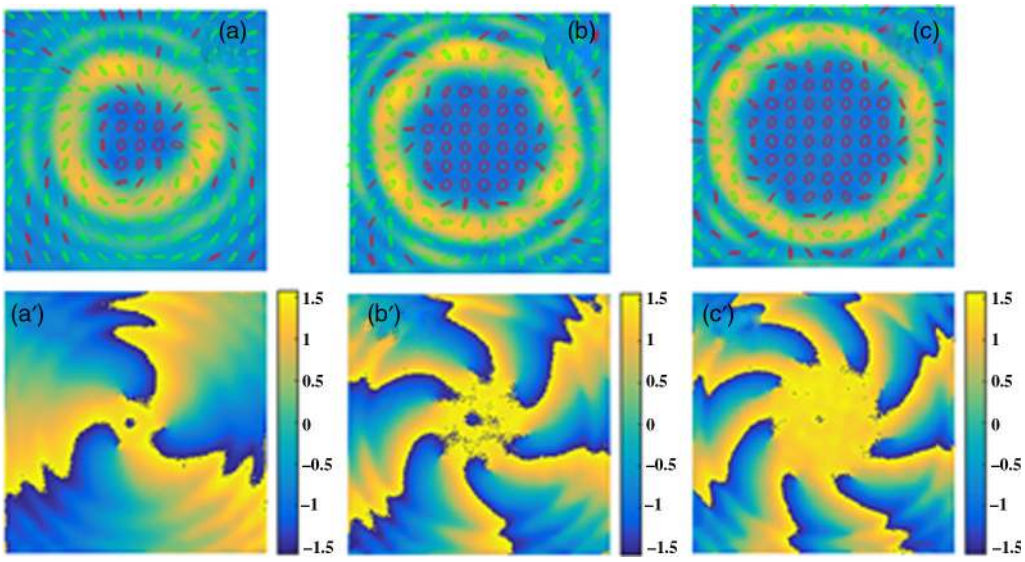

Fig. 33 (a)–(c) Higher-order PS beams generated using LCoS SLM; (a')–(c') corresponding phase maps.

3 Detection of Optical Beams Carrying Orbital Angular Momentum

Modal weights of a complex beam can be calculated either by mode sorting or by modal decomposition. Mode sorting methods result in the physical separation of eigenmodes using active or passive techniques. Modal decomposition, on the other hand, quantifies the different modes present, without necessarily separating them. A variety of methods, involving interferometers,[193] holograms,[54] and Q-plates[194] have been used to carry out mode sorting. However, all these methods are limited by their throughput, i.e., they can detect only one mode at a time.

Cascaded beam splitters and photonic integrated circuits[14] are some of the existing methods that simultaneously identify multiple azimuthal mode components of an input beam but are not efficient and often require careful alignment. For example, the work carried out by Leach et al.[195] looked at sorting at the single-photon level, using a Mach–Zehnder interferometer (MZI). The interferometer was modified such that each arm contained a Dove prism. Sorting was achieved by maintaining an angle θ between the two Dove prisms. This resulted in a phase difference of $2\ell\theta$ between the two arms of the interferometer, where ℓ is the charge of the incoming beam. This setup was able to separate the even and odd modes since a value of $\theta = 90$ deg resulted in constructive interference at one of the interferometer output ports for all even values of ℓ and similar constructive interference at the other port for all odd values of ℓ. By using several cascaded interferometers with different phase differences between each interferometers pair of Dove prisms, a finer sorting could be carried out. Theoretically, this could be achieved with high efficiency. However, the large number of interferometers makes this system both error-prone and cumbersome. The MZI–Dove prism combination was also used by Gao et al.[196] However, instead of cascading interferometers, they used a binary amplitude grating in each output arm of the MZI. The gratings were designed such that if the diffractive order and the angular quantum number were the inverse of each other, the incident helical beam was converted to a Gaussian beam (i.e., it focused to a spot, rather than a ring). From the location of the focus spot along a plane, one could tell the charge of the mode. However, this worked only for a small range of ℓ values. Lavery et al.[193] also extended the idea of cascaded interferometers to finely sort the OAM modes. Each interferometer was constructed in a robust manner that eliminated several of the alignment issues of the original work.

Q-plates have also been used to sort OAM states.[194] Q-plates of topological charge q allow the generation of light beams carrying an OAM of $\pm 2q\hbar$ per photon, with the OAM sign controlled by the input polarization state. Two input OAM states to be sorted (say, $l = \pm 2$) are generated using an SLM and are propagated through a (quarter waveplate (QWP) to generate two orthogonal polarizations, say the right and left circular states. The four photons states thus

generated ($|L,2>, |L,-2>, |R,2>, |R,-2>$) are passed through a Q-plate, $q = 1$, converting them into the states ($|R,4>, |R,0>, |L,0>, |L,-4>$). A second QWP converts the states to ($|H,4>, |H,0>, |V,0>, |V,-4>$), and a polarization beam splitter directs the horizontal and vertical polarization components into transmitted and reflected paths, respectively.

The two modes are separated in the far field by taking advantage of the different radial distributions of the $m = 0$ and 4 modes. This method allows the sorting of only four modes obtained by combining two OAM modes and two orthogonal polarization modes at a time. Also, the radial mode overlap leads to some energy of each mode going into the "wrong" OAM mode.

3.1 *Geometric Transformation Method*

One sorting technique that is used to find the weights of individual modes present in the incident beam is based on a Cartesian to log-polar transformation.[197,198] While this is an elegant method, it has some drawbacks, such as the limited range of azimuthal order modes that it can sort at a time and its inability to determine the weights of radial order modes. Owing to the use of two active LCoS devices, the overall efficiency was also quite poor. However, it is one of the most popular techniques used currently, with the lossy LCoS devices replaced either by diffractive or by refractive elements. The method is described in detail below.

This method is based on the fact that a set of superimposed plane waves propagating with different wave vectors can be focused into distinguishable spots at the focal plane of a convex lens, provided that each sees an additional phase shift that is a multiple of 2π across the lens. This is to ensure that the difference in spot position is comparable to the Rayleigh resolution limit.[199,200] The location of the spot depends on the topological charge of the OAM mode (Fig. 34).

The basis of this sorting technique is the conversion of OAM into linear momentum. The method requires two elements. The first unwraps the phase profile of an OAM mode azimuthally along the ring-shaped nonzero intensity region. Modes with higher azimuthal index number correspond to plane waves with larger wave vector.

The unwrapping operation is carried out by an optical log-polar transformation.[201] The amplitude of the unwrapped beam is obtained at the Fourier plane of the transformation element. The residual phase distortion introduced by the transformation element is compensated by a second element that provides the required phase correction at the Fourier plane to retrieve the phase ramp of the unwrapped beam. The setup is completely reversible, which means that a spatial array of Gaussian focal spots at the focal plane of the lens will be converted into superimposed plane waves with different tilt. These beams then pass through the phase corrector and the transformation element to produce multiplexed OAM beams. The phase profile of the transformation element $\theta_1(x;y)$ and phase correction element $\theta_2(u;v)$ are given as[202,203]

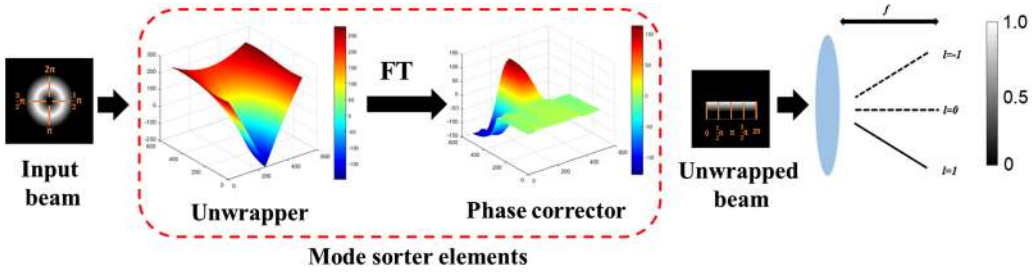

Fig. 34 Configuration of an optical log-polar transformation-based mode sorter and its working principle. The leftmost image indicates the input, which could be the superposition of a number of OAM beams of different charges. This goes through the first element of the log-polar transformation, which unwraps the azimuthal phase profile of the OAM mode. The second phase element lies at the Fourier transform plane and provides the necessary phase correction that allows focusing of the beam into spots for each OAM present in the incident beam. This is indicated on the rightmost part of the figure. The color map of the two phase elements indicates the phase variation across the elements, with blue being 0 and red having the value 2π.

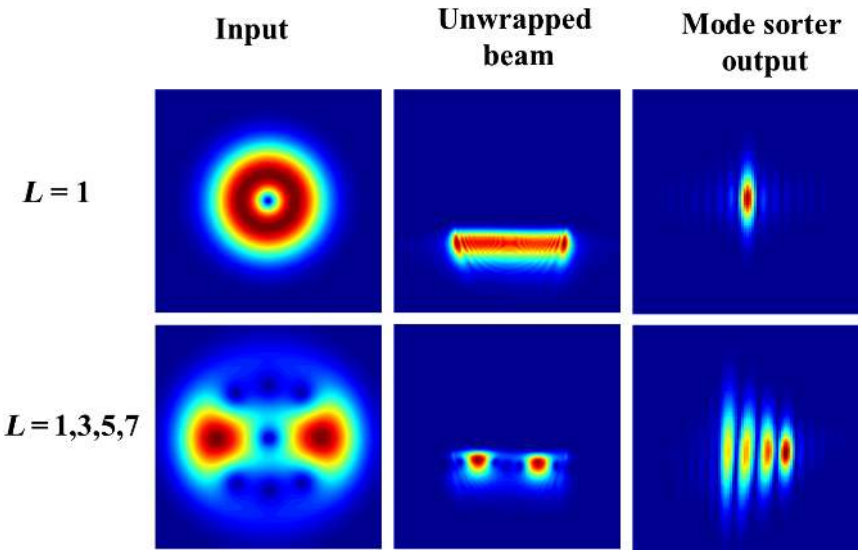

Fig. 35 The simulation results for various OAM mode inputs.

$$\theta_1(x,y) = \tfrac{2\pi}{\lambda}\tfrac{a}{f}\left[y\,\arctan(y/x) - x\,\ln\left(\frac{\sqrt{x^2+y^2}}{b}\right) + x\right], \tag{13}$$

$$\theta_2(u,v) = \tfrac{-2\pi}{\lambda}\tfrac{ab}{f}\left[\exp(-u/a)\cos(v/a)\right]. \tag{14}$$

The parameter d defines the length of the unwrapped beam and is selected such that the unwrapped beam covers 80% of the width of the corrector. The parameter $a = d/2\pi$ ensures that the unwrapped beam is fully mapped on the width of d. The parameter b allows independent control of the translation of the unwrapped beam in the u direction. The f is the focal length of the Fourier transforming lens used. Figure 35 illustrates the results of simulation carried out to demonstrate the demultiplexing process.

One limitation of this method is that there will be a slight overlap of OAM mode content in the output, especially while sorting consecutive OAM modes. This limits the use of this system for single-photon applications. However, the resolution can be improved by incorporating a fan-out element at the output of unwrapper and phase corrector element, followed by a fan-out phase correction element. Therefore, four optical elements are required to improve the resolution. Recent research work[204] has demonstrated that the fan-out element can be integrated along with the phase profile of the transformation element that creates multiple coherent copies of the unwrapped beam at the Fourier plane of the unwrapper. The second element has to correct the relative phase between these copies at the Fourier plane of the fan-out element.[205–207] Recent research work has also demonstrated that performing a spiral transformation instead of a log-polar transformation can also improve the resolution of the mode-sorter output.[208] However, all these methods improve resolution at the expense of making the setup more complex.

The log-polar technique has proved to be one of the most used methods of carrying out mode sorting. While refractive elements are the most efficient, most researchers use phase diffractive elements. These elements are either LC SLMs or elements fabricated using a variety of lithography and etching techniques. Although the log-polar optical transformation is efficient, the need for two elements to complete the demultiplexing still makes the entire operation occupy a large footprint. Extensions to this work, therefore, focused on miniaturing the setup, by integrating the two optical components into a single DOE.[204,209] This was achieved with a neat but simple trick. As the geometric transformation element acts on a ring of light, the central part of the element is unused. This region was filled with the second element structure. In other words, the first element occupied the outer ring of the new combined DOE, whereas the second one lay at the center. The light that had traversed the first element (outer ring) was reflected and made to travel through the second element (central region).

3.2 *Optical Correlation Technique*

In contrast to the mode-sorting techniques outlined above, modal decomposition techniques create a representation of the complex beam as a linear summation of the eigenmodes. Some of the modal decomposition techniques include the spatial and spectral (S^2) imaging technique,[210] numerical methods,[211,212] phase extraction methods,[213,214] and the optical correlation technique.[74,215,216] The relative merits of these techniques are mentioned below.

The S^2 imaging technique involves a complex experimental setup (broadband source or tunable laser, optical spectrum analyzer, and a two-axis mechanical shifter) and requires a long measurement time.[210] The crucial element of numerical method-based modal decomposition is the optimization algorithm such as the Gerchberg–Saxton algorithm,[211] stochastic parallel gradient descent algorithm,[212] and hybrid genetic algorithm.[217] These optimization algorithms easily suffer from initial value sensitivity and local minima problems. The ring technique is one of the modal decomposition techniques, which does not use any optimization algorithm.[218] However, the drawback of this technique is it works only for the zero radial order OAM modes.

Phase extraction methods, such as phase-shifting digital holography,[213] require a reference beam to extract the phase structure of the complex field. Primary limitations of this technique are that it requires a stable interferometric setup and a coherent laser source at the receiver end. On the other hand, optical correlation-based modal decomposition has been demonstrated to address a wide range of the spectrum, although the accuracy may be limited by the specific algorithm that is used. For example, Xie et al.[219] experimentally demonstrated the 15-dB power extinction between the zeroth and first radial order LG modes using an optical correlation technique. The power extinction in their demonstration is limited by the fact that they have used only the phase structure of the LG modes in the decomposition process. Optical correlation-based modal decomposition considering both amplitude and phase structures gives accurate modal weights of the complex beam. Such a technique has been employed to find the modal weights of the optical fiber output in the LP basis.[215] This optical correlation technique can also be used to find the weights of an optical fiber output in OAM basis having both azimuthal and radial order modes. As discussed previously, OAM and SAM are coupled together for fiber modes. Hence, in order to implement optical correlation, OAM and SAM have to be decoupled.

In this section, we discuss optical correlation techniques for scalar OAM modes. It should be noted that any scalar light beam (U) can be represented by a superposition of $LG_{l,p}$ modes with corresponding complex weights $W_{l,p}$, as shown in Eq. (15). The complex weight of a mode is calculated by optically correlating the input beam with the complex conjugate of the mode, as shown in Eq. (16).

$$U = \sum_{l,p} W_{l,p} LG_{l,p}, \tag{15}$$

$$W_{l,p} = \iint_{l,p} ULG^{*}_{l,p} W_{l,p} r \mathrm{d}r\, \mathrm{d}\phi. \tag{16}$$

Equation (16) is essentially a dot-product operation between the input beam and the complex conjugate of the mode. This operation is performed experimentally by using an SLM and a convex lens.[220]

The input beam $LG_{l,p}$ is multiplied with its complex conjugate mode using an SLM by encoding necessary holograms. To perform the integral operation, the reflected beam is propagated through the convex lens. The electric field corresponding to the reflected beam at the Fourier plane of the convex lens is given in Eq. (17).[57,220]

$$U_f(u,v) = \frac{\exp(ikf)\exp(ikr^2/2f)}{i\lambda f} \iint ULG^{*}_{l,p} \exp\left[-\frac{i2\pi\rho r}{\lambda f}\cos(\Theta-\phi)\right]\rho \mathrm{d}\rho\, \mathrm{d}\phi, \tag{17}$$

where $r = \sqrt{u^2+v^2}$, $\Theta = \tan^{-1}(u,v)$, u, and v are the spatial frequencies, f is the focal length of the convex lens, λ is the wavelength, and k is the propagation constant of the beam.

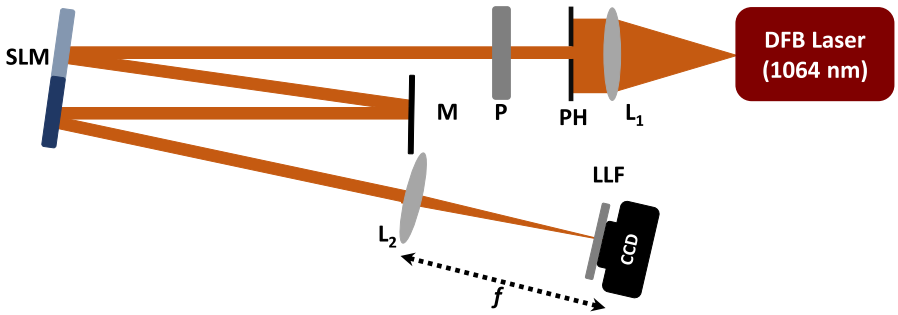

Fig. 36 Experimental setup for implementing the optical correlation technique. DFB, distributed feedback laser; L_1 (focal length = 10 cm) and L_2 (focal length = 20 cm), convex lens; PH, pinhole; P, polarizer; SLM, spatial light modulator; M, mirror; LLF, laser line filter at 1064 nm; CCD, charge-coupled device camera.

The center of the Fourier plane $U_f(0,0)$, which is commonly referred as the DC component, gives the weight of the $LG_{l,p}$ mode. Since the camera captures the intensity, the square root of the observed intensity is calculated to obtain the field weight. However, it should be noted that the phase information of the beam is lost in this process and, as such, the relative phase between different modes is not considered.

Based on the above optical correlation algorithm, modal decomposition of azimuthal, as well as radial order LG modes, is performed. The schematic of the experimental setup used for implementing the optical correlation technique is shown in Fig. 36.[220] One half of the SLM is programmed to generate the required LG beam and the other half is programmed to perform the dot-product operation as part of the modal decomposition.

In the above experiments, high extinction (27 dB, limited by the camera bit resolution) between the matched and the orthogonal cases are achieved when two radial order modes ($p = 0, 1$) with two azimuthal order modes ($l = 0, 1$) are used. To explore the scalability to higher-order modes, the above optical correlation experiments are extended to higher azimuthal order modes ($l = -4$ to $+4$). The observations from such experiments are summarized using a parity plot, as shown in Fig. 37.[220] For simplicity, a constant decomposition CGH radius R of 1.0 mm is used for these experiments. The diagonal elements of the parity plot represent the power measured when the generated and decomposition CGH corresponding to LG modes are matched and the off-diagonal elements represent the power coupled to neighboring modes. The observations from Fig. 37 are the following: when LG modes with $p = 0$ and $l = -4$ to $+4$ are generated and correlated with matched decomposition CGH patterns (corresponding to diagonal values in Q1 quadrant), the normalized power is uniform and maximum. However, a finite amount of power is observed when correlated with the orthogonal $p = 1$ decomposition CGH patterns (corresponding to diagonal values in Q2). For $l = 0$ mode, an extinction of $\approx$23 dB is observed. This degradation of extinction compared to an expected value of 27 dB is due to the nonoptimal decomposition CGH radius of 1 mm used in the above measurements. Furthermore, an increase in the power measured is observed as we increase the azimuthal number (l). For example, when LG_{-40} is generated, we noticed only 15.5 dB extinction between LG_{-40} and LG_{-41} modes. This degradation in extinction for higher-order azimuthal modes is once again attributed to the wavefront aberration introduced by the SLM, as well as the associated optics, for a beam of higher-order transverse mode such as the LG modes studied here.[221,222]

Interestingly, when LG modes with $p = 1$ are generated, the power coupling to the $p = 0$ LG modes is much lower (extinction of 27 dB, corresponding to diagonal values in Q4). Specifically, when LG_{-41} is generated, 27-dB extinction between LG_{-41} and LG_{-40} modes is observed (which is better than the converse case). This is not surprising since the optimal decomposition CGH radius is used for this case compared to the above case.

It should be noted that a similar optical correlation technique has been reported recently by other groups. A collinear phase-shifting holographic method[213] is reported with a modal extinction ratio of 24 dB between LG_{10} and LG_{11}. Another optical correlation technique based on

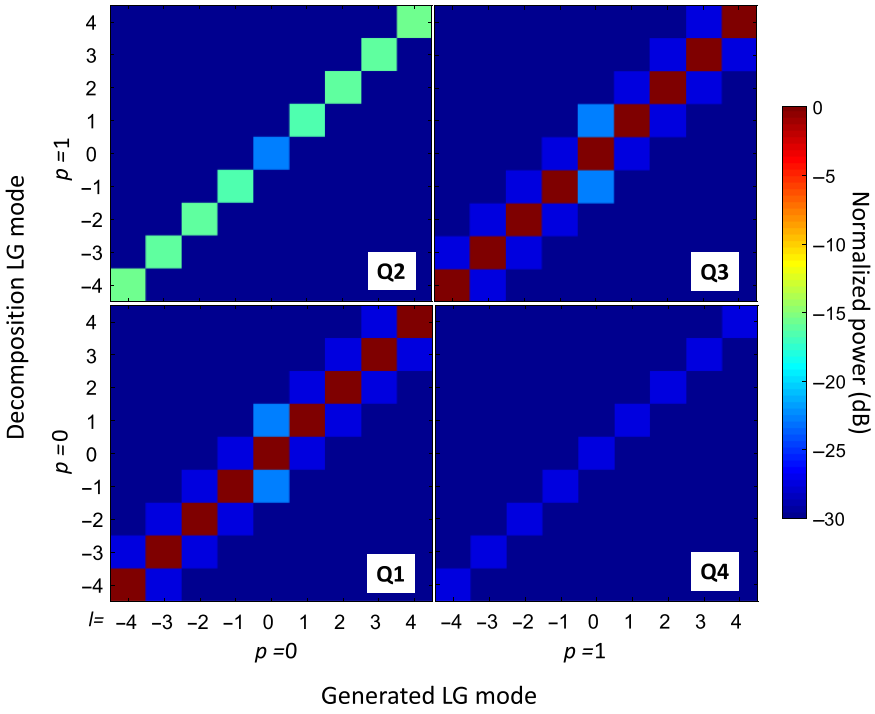

Fig. 37 Normalized power measured from optical correlation technique for different combinations of generated and decomposition *LG* modes with radial mode order $p = 0$, 1 and azimuthal mode order $l = -4$ to $+4$. Diagonal elements represent parity and the off-diagonal elements represent the magnitude of coupling to neighboring modes. Q1–Q4 corresponds to the different quadrants in the above plot.

a phase-retrieval method[223] is reported for decomposing $LG_{lp}(l = 0, 0 \leq p \leq 2)$ modes with <10 dB modal extinction ratio between the mode of interest and the neighboring modes. An optical correlation technique based on intensity flattening[224] is reported for decomposing $LG_{lp}(l = 0, 0 \leq p \leq 7)$ radial order modes. Unfortunately, modal extinction ratios of the decomposed modes are not presented in the article. A maximum visibility (ratio of the power in the desired mode to the power in all the modes) of 99.1% is reported. Finally, a radial mode sorter[225] has been reported for decomposing $LG_{lp}(-2 \leq l \leq 2, 0 \leq p \leq 1)$ modes with a maximum modal extinction ratio of 10 dB.

In comparison to the above methods, our method is tested for $LG_{l,p}(-4 \leq l \leq 4, 0 \leq p \leq 1)$ modes having both azimuthal and radial orders.[220] A modal extinction ratio of 27 dB is obtained (limited by our camera resolution), irrespective of the input mode, which is greater than any of the extinction ratios of the above-mentioned schemes. A visibility of 99.9% is obtained in our experiments,[220] which is also greater than the visibility obtained in the optical correlation technique based on intensity flattening.[224]

So far, modal decomposition using an optical correlation algorithm is discussed for the case wherein only a single mode is generated. In several practical applications, including MDM systems, modal decomposition has to be performed for composite (two or more) modes. As such, the above investigation is extended to the case of a composite beam consisting of 10 different LG modes (azimuthal mode indices $l = -2$ to $+2$ and radial mode indices $p = 0$, 1). A sample modal distribution is chosen such that the generated mode weights (denoted as markers in Fig. 38[220]) are halved for consecutive azimuthal mode index (both positive and negative values). As in the above case, the decomposed modal weights agree well with the generated modal weights across the entire mode spectrum. The relatively high error observed for the LG_{-20} and LG_{20} modes are due to the nonoptimal radius of the decomposition CGH, as explained previously. However, the intensity structure of the reconstructed beam [illustrated in Fig. 38(c)] based on the experimentally obtained modal weights closely resembles the generated composite beam of Fig. 38(a).

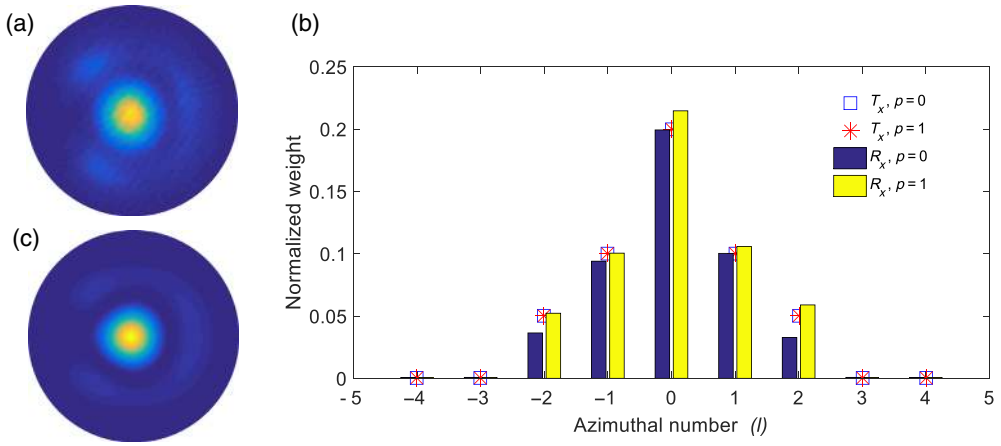

Fig. 38 (a) Intensity structure of the generated composite beam consisting of 10 *LG* modes. (b) Weights of the generated (markers) and decomposition (bars) *LG* mode spectrum for radial orders $p = 0, 1$ plotted as a function of different azimuthal mode indices $l = -4$ to $+4$. (c) Intensity structure simulated using the experimentally obtained modal weights.

4 Summary and Conclusions

Light beams with spin and OAM and arising due to SOI are so diverse and are emerging so rapidly that an overview once every few years has become a norm and well deserving. This review article is an attempt to classify this area of research from a point of view that addresses the needs of scientists and engineers who want to generate/detect AM modes and are looking for the best technique for their desired application. Such applications may be in microscopy, classical-quantum optical communications, or simply to explore light–matter interactions in different physical–chemical–biological and engineering systems, wherein this new DoF of light beam can provide additional and so far hidden information. To this end, we presented several passive and active spatial light modulation techniques to generate or detect optical beams with AM through manipulation of amplitude, phase, and polarization across the optical beam.

In this review paper, we have elucidated the various approaches previously reported for generating light beams with OAM through spatial light modulation. One class of SLMs relies on manipulating the phase across the optical beam. Examples of such an approach include the use of refractive SPPs, blazed and DOEs, HOEs, and more lately, the use of all-dielectric metasurfaces. Manipulation of the amplitude across the optical beam through SLMs, such as DMDs, is another important approach that has been discussed in our paper. Recently, there has been significant interest on the use of OAM modes for high capacity MDM optical communication systems. For such an application, a hybrid all-fiber fused coupler approach may provide a robust platform, and we have discussed the key principles for this approach. Finally, we have discussed the generation of vector-vortex modes, which once again is attractive for classical and quantum optical communication applications.

In many of the above applications, a key issue is the detection of the OAM mode spectrum at the optical receiver. From this perspective, we have presented a couple of promising approaches, including sorting using geometric transformation and decomposition using optical correlation technique. Although it is difficult to identify a particular approach as the best for any given application, the discussion presented in this review is intended to provide interested scientists and engineers the key information required to make a wise choice on the approach best suited for their application.

Acknowledgments

R. D. thanks his co-supervisor Professor Saulius Juodkazis at Swinburne University and the joint doctoral program between IIT Madras and Swinburne University. N. K. V. gratefully acknowledges the financial support from Science and Engineering Research Board (SERB), Department of Science and Technology (DST), India, for this and all related work. Balaji and Srinivas

acknowledge technical inputs from Shankar Pidishety and Gilberto Brambilla, ORC, University of Southampton. Research and understanding contributions of all past and present research students of the group are also acknowledged. SB thanks her fellow authors of Ref. 53 for the work leading to Figs. 7 and 15. S. B. also thanks the Department of Science and Technology for funding some of the work reported in this paper though Grant No. DST/IMRCD/BRICS/Pilotcall1/OPTIMODE/2017.

References

1. J. H. Poynting, "The wave motion of a revolving shaft, and a suggestion as to the angular momentum in a beam of circularly polarised light," *Proc. R. Soc. Lond. Ser. A* **82**(557), 560–567 (1909).
2. L. Allen et al., "Orbital angular momentum of light and the transformation of Laguerre–Gaussian laser modes," *Phys. Rev. A* **45**(11), 8185–8189 (1992).
3. M. Soskin and M. Vasnetsov, "Singular optics," *Prog. Opt.* **42**(4), 219–276 (2001).
4. A. Bekshaev, M. Soskin, and M. Vasnetsov, "Paraxial light beams with angular momentum," arXiv:0801.2309 (2008).
5. D. L. Andrews, *Structured Light and Its Applications: An Introduction to Phase-structured Beams and Nanoscale Optical Forces*, Academic Press, Amsterdam (2011).
6. M. W. Beijersbergen et al., "Astigmatic laser mode converters and transfer of orbital angular momentum," *Opt. Commun.* **96**(1–3), 123–132 (1993).
7. A. M. Yao and M. J. Padgett, "Orbital angular momentum: origins, behavior and applications," *Adv. Opt. Photonics* **3**(2), 161–204 (2011).
8. D. McGloin and K. Dholakia, "Bessel beams: diffraction in a new light," *Contemp. Phys.* **46**(1), 15–28 (2005).
9. J. C. Gutiérrez-Vega, M. Iturbe-Castillo, and S. Chávez-Cerda, "Alternative formulation for invariant optical fields: Mathieu beams," *Opt. Lett.* **25**(20), 1493–1495 (2000).
10. M. A. Bandres and J. C. Gutiérrez-Vega, "Ince–Gaussian beams," *Opt. Lett.* **29**(2), 144–146 (2004).
11. E. Karimi et al., "Hypergeometric-Gaussian modes," *Opt. Lett.* **32**(21), 3053–3055 (2007).
12. A. Y. Bekshaev and A. Karamoch, "Spatial characteristics of vortex light beams produced by diffraction gratings with embedded phase singularity," *Opt. Commun.* **281**(6), 1366–1374 (2008).
13. L. Zhu et al., "18 km low-crosstalk OAM+ WDM transmission with 224 individual channels enabled by a ring-core fiber with large high-order mode group separation," *Opt. Lett.* **43**(8), 1890–1893 (2018).
14. A. E. Willner et al., "Optical communications using orbital angular momentum beams," *Adv. Opt. Photonics* **7**(1), 66–106 (2015).
15. J.-M. Liu, *Photonic Devices*, Cambridge University Press, Cambridge (2009).
16. S. Ramachandran and P. Kristensen, "Optical vortices in fiber," *Nanophotonics* **2**(5–6), 455–474 (2013).
17. S. W. Hell and J. Wichmann, "Breaking the diffraction resolution limit by stimulated emission: stimulated-emission-depletion fluorescence microscopy," *Opt. Lett.* **19**(11), 780–782 (1994).
18. L. Yan et al., "Q-plate enabled spectrally diverse orbital-angular-momentum conversion for stimulated emission depletion microscopy," *Optica* **2**(10), 900–903 (2015).
19. J. R. Moffitt, C. Osseforth, and J. Michaelis, "Time-gating improves the spatial resolution of STED microscopy," *Opt. Express* **19**(5), 4242–4254 (2011).
20. S. Safdar et al., "Finite element simulation of laser tube bending: effect of scanning schemes on bending angle, distortions and stress distribution," *Opt. Laser Technol.* **39**(6), 1101–1110 (2007).
21. M. Gecevičius et al., "Single beam optical vortex tweezers with tunable orbital angular momentum," *Appl. Phys. Lett.* **104**(23), 231110 (2014).
22. M. P. Lavery et al., "Observation of the rotational Doppler shift of a white-light, orbital-angular-momentum-carrying beam backscattered from a rotating body," *Optica* **1**(1), 1–4 (2014).

23. G. A. Swartzlander et al., "Astronomical demonstration of an optical vortex coronagraph," *Opt. Express* **16**(14), 10200–10207 (2008).
24. M. Erhard et al., "Twisted photons: new quantum perspectives in high dimensions," *Light Sci. Appl.* **7**(3), 17146 (2018).
25. N. Bozinovic et al., "Orbital angular momentum (OAM) based mode division multiplexing (MDM) over a km-length fiber," in *Eur. Conf. and Exhib. on Opt. Commun.*, Optical Society of America, p. Th.3.C6 (2012).
26. G. Milione et al., "Orbital-angular-momentum mode (de) multiplexer: a single optical element for MIMO-based and non-MIMO-based multimode fiber systems," in *OFC 2014*, IEEE, pp. 1–3 (2014).
27. G. C. Berkhout et al., "Measuring orbital angular momentum superpositions of light by mode transformation," *Opt. Lett.* **36**(10), 1863–1865 (2011).
28. C. Schulze et al., "Wavefront reconstruction by modal decomposition," *Opt Express* **20**(18), 19714–19725 (2012).
29. D. Flamm et al., "Fast M2 measurement for fiber beams based on modal analysis," *Appl. Opt.* **51**(7), 987–993 (2012).
30. D. Flamm et al., "Modal characterization of fiber-to-fiber coupling processes," *Opt. Lett.* **38**(12), 2128–2130 (2013).
31. J. D. B. De La Tocnaye and L. Dupont, "Complex amplitude modulation by use of liquid-crystal spatial light modulators," *Appl. Opt.* **36**(8), 1730–1741 (1997).
32. J. A. Davis et al., "Complete polarization control of light from a liquid crystal spatial light modulator," in *Front. in Opt.*, Optical Society of America, p. FTu1F.4 (2012).
33. A. Friesem, A. Kozma, and G. Adams, "Recording parameters of spatially modulated coherent wavefronts," *Appl. Opt.* **6**(5), 851–856, 1967.
34. E. Van Putten, I. M. Vellekoop, and A. Mosk, "Spatial amplitude and phase modulation using commercial twisted nematic LCDs," *Appl. Opt.* **47**(12), 2076–2081 (2008).
35. M. Plewicki et al., "Independent control over the amplitude, phase, and polarization of femtosecond pulses," *Appl. Phys. B* **86**(2), 259–263 (2007).
36. L. Liu et al., "Broadband metasurfaces with simultaneous control of phase and amplitude," *Adv. Mater.* **26**(29), 5031–5036 (2014).
37. C. Pfeiffer and A. Grbic, "Cascaded metasurfaces for complete phase and polarization control," *Appl. Phys. Lett.* **102**(23), 231116 (2013).
38. V. Bagnoud and J. D. Zuegel, "Independent phase and amplitude control of a laser beam by use of a single-phase-only spatial light modulator," *Opt. Lett.* **29**(3), 295–297 (2004).
39. E. H. Waller and G. von Freymann, "Independent spatial intensity, phase and polarization distributions," *Opt. Express* **21**(23), 28167–28174 (2013).
40. S. Liu et al., "Highly efficient generation of arbitrary vector beams with tunable polarization, phase, and amplitude," *Photonics Res.* **6**(4), 228–233 (2018).
41. B. H. Ong et al., "Photothermally enabled lithography for refractive-index modulation in su-8 photoresist," *Opt. Lett.* **31**(10), 1367–1369 (2006).
42. J. Yu et al., "Modulation of refractive index and thickness of poly (methyl methacrylate) thin films with UV irradiation and heat treatment," *Appl. Surf. Sci.* **252**(5), 1283–1292 (2005).
43. A. Vijayakumar and S. Bhattacharya, *Design and Fabrication of Diffractive Optical Elements with MATLAB*, SPIE Press, Bellingham, Washington, DC (2017).
44. M. Beijersbergen et al., "Helical-wavefront laser beams produced with a spiral phaseplate," *Opt. Commun.* **112**(5–6), 321–327 (1994).
45. K. Sueda et al., "Laguerre–Gaussian beam generated with a multilevel spiral phase plate for high intensity laser pulses," *Opt. Express* **12**(15), 3548–3553 (2004).
46. V. V. Kotlyar et al., "Generation of phase singularity through diffracting a plane or Gaussian beam by a spiral phase plate," *J. Opt. Soc. Am. A* **22**(5), 849–861 (2005).
47. W. Lee, X.-C. Yuan, and W. Cheong, "Optical vortex beam shaping by use of highly efficient irregular spiral phase plates for optical micromanipulation," *Opt. Lett.* **29**(15), 1796–1798 (2004).
48. S. Oemrawsingh et al., "Production and characterization of spiral phase plates for optical wavelengths," *Appl. Opt.* **43**(3), 688–694 (2004).

49. T. Watanabe et al., "Generation of a doughnut-shaped beam using a spiral phase plate," *Rev. Sci. Instrum.* **75**(12), 5131–5135 (2004).
50. C. Jun et al., "Generation of optical vortex using a spiral phase plate fabricated in quartz by direct laser writing and inductively coupled plasma etching," *Chin. Phys. Lett.* **26**(1), 014202 (2009).
51. W. Cheong et al., "Direct electron-beam writing of continuous spiral phase plates in negative resist with high power efficiency for optical manipulation," *Appl. Phys. Lett.* **85**(23), 5784–5786 (2004).
52. V. Pramitha, A. Vijayakumar, and S. Bhattacharya, "Fabrication of multilevel spiral phase plates by focused ion beam milling," *Proc. SPIE* **8769**, 87691S (2013).
53. P. Vayalamkuzhi et al., "Direct patterning of vortex generators on a fiber tip using a focused ion beam," *Opt. Lett.* **41**(10), 2133–2136 (2016).
54. A. Vijayakumar et al., "Generation of structured light by multilevel orbital angular momentum holograms," *Opt. Express* **27**(5), 6459–6470 (2019).
55. R. Dharmavarapu, S. Bhattacharya, and S. Juodkazis, "GDOESII: software for design of diffractive optical elements and phase mask conversion to GDSII lithography files," *SoftwareX* **9**, 126–131 (2019).
56. D. C. O'Shea et al., *Diffractive Optics: Design, Fabrication, and Test*, Vol. **62**, SPIE Press, Bellingham, Washington, DC (2004).
57. J. W. Goodman, *Introduction to Fourier Optics*, Roberts and Company Publishers, Englewood, Colorado (2005).
58. P. Hariharan and P. Hariharan, *Optical Holography: Principles, Techniques and Applications*, Cambridge University Press, Cambridge (1996).
59. T.-C. Poon and J.-P. Liu, *Introduction to Modern Digital Holography: with MATLAB*, Cambridge University Press, Cambridge (2014).
60. B. R. Brown and A. W. Lohmann, "Complex spatial filtering with binary masks," *Appl. Opt.* **5**(6), 967–969 (1966).
61. O. Bryngdahl and F. Wyrowski, "I digital holography-computer-generated holograms," *Prog. Opt.* **28**, 1–86 (1990).
62. G. Tricoles, "Computer generated holograms: an historical review," *Appl. Opt.* **26**(20), 4351–4360 (1987).
63. Z. Sacks, D. Rozas, and G. Swartzlander, "Holographic formation of optical-vortex filaments," *J. Opt. Soc. Am. B* **15**(8), 2226–2234 (1998).
64. I. Sola et al., "High power vortex generation with volume phase holograms and non-linear experiments in gases," *Appl. Phys. B* **91**(1), 115–118 (2008).
65. A. Y. Bekshaev et al., "Generation of optical vortex light beams by volume holograms with embedded phase singularity," *Opt. Commun.* **285**(20), 4005–4014 (2012).
66. A. Bekshaev et al., "Optical vortex generation by volume holographic elements with embedded phase singularity: effects of misalignments," *Ukrainian J. Phys. Opt.* **14**(4), 171–186 (2013).
67. S. Tao et al., "Sequence of focused optical vortices generated by a spiral fractal zone plate," *Appl. Phys. Lett.* **89**(3), 031105 (2006).
68. N. Gao et al., "Square optical vortices generated by binary spiral zone plates," *Appl. Phys. Lett.* **98**(15), 151106 (2011).
69. V. Y. Bazhenov, M. Vasnetsov, and M. Soskin, "Laser beams with screw dislocations in their wavefronts," *JETP Lett.* **52**(8), 429–431 (1990).
70. V. Y. Bazhenov, M. Soskin, and M. Vasnetsov, "Screw dislocations in light wavefronts," *J. Mod. Opt.* **39**(5), 985–990 (1992).
71. N. Heckenberg et al., "Generation of optical phase singularities by computer-generated holograms," *Opt. Lett.* **17**(3), 221–223 (1992).
72. L. Janicijevic and S. Topuzoski, "Fresnel and Fraunhofer diffraction of a Gaussian laser beam by fork-shaped gratings," *J. Opt. Soc. Am. A* **25**(11), 2659–2669 (2008).
73. L. Yi-Dong, G. Chun-Qing, and G. Ming-Wei, "Study on holographic grating diffraction for Laguerre–Gaussian beam generation," *Chin. Phys. B* **17**(5), 1769–1776 (2008).
74. A. Forbes, A. Dudley, and M. McLaren, "Creation and detection of optical modes with spatial light modulators," *Adv. Opt. Photonics* **8**(2), 200–227 (2016).

75. L. Stoyanov et al., "Far field diffraction of an optical vortex beam by a fork-shaped grating," *Opt. Commun.* **350**, 301–308 (2015).
76. B. Jackin and P. Palanisamy, "A completely open source based computing system for computer generation of Fourier holograms," *Comput. Phys. Commun.* **180**(10), 1882–1887 (2009).
77. A. Vijayakumar, B. Jackin, and P. Palanisamy, "Computer generated Fourier holograms for undergraduate optics laboratory," *Phys. Educ.* **28**(4), 4 (2012).
78. S. Khonina et al., "Trochoson," *Opt. Commun.* **91**(3–4), 158–162 (1992).
79. C. Paterson and R. Smith, "Higher-order Bessel waves produced by axicon-type computer-generated holograms," *Opt. Commun.* **124**(1–2), 121–130 (1996).
80. S. Qiong-Ge et al., "Generalization and propagation of spiraling Bessel beams with a helical axicon," *Chin. Phys. B* **21**(1), 014208 (2012).
81. F. Saad, E. El Halba, and A. Belafhal, "Generation of generalized spiraling Bessel beams of arbitrary order by curved fork-shaped holograms," *Opt. Quantum Electron.* **48**(10), 454 (2016).
82. A. Matijošius, V. Jarutis, and A. Piskarskas, "Generation and control of the spiraling zero-order Bessel beam," *Opt. Express* **18**(9), 8767–8771 (2010).
83. J. Zhao et al., "Curved singular beams for three-dimensional particle manipulation," *Sci. Rep.* **5**, 12086 (2015).
84. S. Chávez-Cerda et al., "Holographic generation and orbital angular momentum of high-order Mathieu beams," *J. Opt. B: Quantum Semiclassical Opt.* **4**(2), S52 (2002).
85. J. Atencia et al., "Holographic optical element to generate achromatic vortices," *Opt. Express* **21**(18), 21056–21061 (2013).
86. J. E. Curtis and D. G. Grier, "Modulated optical vortices," *Opt. Lett.* **28**(11), 872–874 (2003).
87. Q. Sun et al., "Generation of spiraling high-order Bessel beams," *Appl. Phys. B* **104**(1), 215–221 (2011).
88. B. Zhang and D. Zhao, "Focusing properties of Fresnel zone plates with spiral phase," *Opt. Express* **18**(12), 12818–12823 (2010).
89. A. Vijayakumar and S. Bhattacharya, "Design, fabrication, and evaluation of a multilevel spiral-phase Fresnel zone plate for optical trapping," *Appl. Opt.* **51**(25), 6038–6044 (2012).
90. A. Sabatyan and Z. Behjat, "Radial phase modulated spiral zone plate for generation and manipulation of optical perfect vortex," *Opt. Quantum Electron.* **49**(11), 371 (2017).
91. M. K. Karahroudi et al., "Generation of perfect optical vortices using a Bessel–Gaussian beam diffracted by curved fork grating," *Appl. Opt.* **56**(21), 5817–5823 (2017).
92. B. Boruah, "Dynamic manipulation of a laser beam using a liquid crystal spatial light modulator," *Am. J. Phys.* **77**(4), 331–336 (2009).
93. J. Pavlin, N. Vaupotič, and M. Čepič, "Liquid crystals: a new topic in physics for undergraduates," *Eur. J. Phys.* **34**(3), 745–761 (2013).
94. J. A. Davis et al., "Encoding amplitude information onto phase-only filters," *Appl. Opt.* **38**(23), 5004–5013 (1999).
95. L. Zhu and J. Wang, "Arbitrary manipulation of spatial amplitude and phase using phase-only spatial light modulators," *Sci. Rep.* **4**, 7441 (2014).
96. R. W. Gerchberg, "A practical algorithm for the determination of phase from image and diffraction plane pictures," *Optik* **35**, 237–246 (1972).
97. V. Arrizón et al., "Pixelated phase computer holograms for the accurate encoding of scalar complex fields," *J. Opt. Soc. Am. A* **24**, 3500–3507 (2007).
98. V. Arrizón, G. Méndez, and D. Sánchez-de La-Llave, "Accurate encoding of arbitrary complex fields with amplitude-only liquid crystal spatial light modulators," *Opt. Express* **13**(20), 7913–7927 (2005).
99. G. N. Watson, *A Treatise on the Theory of Bessel Functions*, Cambridge University Press, Cambridge (1995).
100. S. Huang et al., "Composite vortex beams by coaxial superposition of Laguerre–Gaussian beams," *Opt. Lasers Eng.* **78**, 132–139 (2016).
101. N. Yu et al., "Light propagation with phase discontinuities: generalized laws of reflection and refraction," *Science* **334**(6054), 333–337 (2011).

102. N. Yu and F. Capasso, "Flat optics with designer metasurfaces," *Nat. Mater.* **13**(2), 139–150 (2014).
103. J. Huang, "Reflect array antenna," in *Encyclopedia of RF and Microwave Engineering* (2005).
104. D. Pozar and T. Metzler, "Analysis of a reflect array antenna using microstrip patches of variable size," *Electron. Lett.* **29**(8), 657–658 (1993).
105. A. E. Minovich et al., "Functional and nonlinear optical metasurfaces," *Laser Photonics Rev.* **9**(2), 195–213 (2015).
106. P. Genevet and F. Capasso, "Holographic optical metasurfaces: a review of current progress," *Rep. Prog. Phys.* **78**(2), 024401 (2015).
107. S. M. Choudhury et al., "Material platforms for optical metasurfaces," *Nanophotonics* **7**(6), 959–987 (2018).
108. K. E. Chong et al., "Efficient polarization-insensitive complex wavefront control using Huygens' metasurfaces based on dielectric resonant meta-atoms," *ACS Photonics* **3**(4), 514–519 (2016).
109. I. Staude et al., "Tailoring directional scattering through magnetic and electric resonances in subwavelength silicon nanodisks," *ACS Nano* **7**(9), 7824–7832 (2013).
110. A. V. Kildishev, A. Boltasseva, and V. M. Shalaev, "Planar photonics with metasurfaces," *Science* **339**(6125), 1232009 (2013).
111. M. Khorasaninejad et al., "Metalenses at visible wavelengths: diffraction-limited focusing and subwavelength resolution imaging," *Science* **352**(6290), 1190–1194 (2016).
112. R. Dharmavarapu et al., "Dielectric cross-shaped resonator based metasurface for vortex beam generation in mid-IR and THz wavelengths," *Nanophotonics* **8**(7), 1263–1270 (2019).
113. S. M. Kamali et al., "Angle-multiplexed metasurfaces: encoding independent wavefronts in a single metasurface under different illumination angles," *Phys. Rev. X* **7**(4), 041056 (2017).
114. T. Qiu et al., "Deep learning: a rapid and efficient route to automatic metasurface design," *Adv. Sci.* **6**(12), 1900128 (2019).
115. L. Li et al., "Machine-learning reprogrammable metasurface imager," *Nat. Commun.* **10**(1), 1082 (2019).
116. P. Genevet et al., "Ultra-thin plasmonic optical vortex plate based on phase discontinuities," *Appl. Phys. Lett.* **100**(1), 013101 (2012).
117. D. Hu et al., "Ultrathin terahertz planar elements," *Adv. Opt. Mater.* **1**(2), 186–191 (2013).
118. J. He et al., "Generation and evolution of the terahertz vortex beam," *Opt. Express* **21**(17), 20230–20239 (2013).
119. R. C. Devlin et al., "Arbitrary spin-to–orbital angular momentum conversion of light," *Science* **358**(6365), 896–901 (2017).
120. F. Yue et al., "Vector vortex beam generation with a single plasmonic metasurface," *ACS Photonics* **3**(9), 1558–1563 (2016).
121. C. Yan et al., "Generation of polarization-sensitive modulated optical vortices with all-dielectric metasurfaces," *ACS Photonics* **6**(3), 628–633 (2019).
122. H. Ren et al., "Metasurface orbital angular momentum holography," *Nat. Commun.* **10**(1), 2986 (2019).
123. R. Dharmavarapu et al., "All-dielectric metasurface for wavefront control at terahertz frequencies," *Proc. SPIE* **10456**, 104561W (2018).
124. J. A. Davis et al., "Analysis of a segmented Q-plate tunable retarder for the generation of first-order vector beams," *Appl. Opt.* **54**(32), 9583–9590 (2015).
125. A. Rubano et al., "Q-plate technology: a progress review," *J. Opt. Soc. Am. B* **36**(5), D70–D87 (2019).
126. M. Beresna, M. Gecevičius, and P. G. Kazansky, "Polarization sensitive elements fabricated by femtosecond laser nanostructuring of glass," *Opt. Mater. Express* **1**(4), 783–795 (2011).
127. M. C. Park et al., "Properties of DMDs for holographic displays," *J. Mod. Opt.* **62**(19), 1600–1607 (2015).

128. Z. Xin, C. Zhang, and X. Yuan, "Concentric perfect optical vortex beam generated by a digital micromirrors device," *IEEE Photonics J.* **9**(2), 1–7 (2017).
129. B. R. Brown and A. W. Lohmann, "Computer-generated binary holograms*," *IBM J. Res. Dev.* **13**(2), 160–168 (1969).
130. A. W. Lohmann and D. P. Paris, "Binary Fraunhofer holograms, generated by computer," *Appl. Opt.* **6**(10), 1739–1748 (1967).
131. R. Piestun, B. Spektor, and J. Shamir, "On-axis binary-amplitude computer generated holograms," *Opt. Commun.* **136**(March), 85–92 (1997).
132. Y. X. Ren et al., "Experimental generation of Laguerre–Gaussian beam using digital micromirror device.," *Appl. Opt.* **49**(10), 1838–1844 (2010).
133. S. A. Goorden, J. Bertolotti, and A. P. Mosk, "Superpixel-based spatial amplitude and phase modulation using a digital micromirror device," *Opt. Express* **22**(15), 17999–18009 (2014).
134. W. H. Lee, "Binary computer-generated holograms," *Appl. Opt.* **18**(21), 3661–3669 (1979).
135. W. H. Lee, "Binary synthetic holograms," *Appl. Opt.* **13**(7), 1677 (1974).
136. R. Ismaeel et al., "All-fiber fused directional coupler for highly efficient spatial mode conversion," *Opt. Express* **22**(10), 11610–11619 (2014).
137. S. Ramachandran, P. Kristensen, and M. F. Yan, "Generation and propagation of radially polarized beams in optical fibers," *Opt. Lett.* **34**(16), 2525–2527 (2009).
138. S. Pidishety et al., "Investigation of scalability of all-fiber fused mode selective coupler for generating multiple OAM states," in *Int. Conf. Fibre Opt. and Photonics*, Optical Society of America, p. W2G.4 (2016).
139. G. Brambilla, "Optical fibre nanowires and microwires: a review," *J. Opt.* **12**(4), 043001 (2010).
140. X. Heng et al., "All-fiber stable orbital angular momentum beam generation and propagation," *Opt. Express* **26**(13), 17429–17436 (2018).
141. J. Wen et al., "All-fiber OAM amplifier with high purity and broadband spectrum gain based on fused taper vortex-beam coupler," *IEEE Photonics J.* **10**(6), 1–8 (2018).
142. J. Yang et al., "All-fiber multiplexing and transmission of high-order circularly polarized orbital angular momentum modes with mode selective couplers," *IEEE Photonics J.* **11**(3), 1–9 (2019).
143. Z. S. Eznaveh et al., "Photonic lantern broadband orbital angular momentum mode multiplexer," *Opt. Express* **26**(23), 30042–30051 (2018).
144. Y. Li et al., "Mode-selective photonic lanterns for orbital angular momentum mode division multiplexing," *Appl. Sci.* **9**(11), 2233 (2019).
145. Q. Zhan, "Cylindrical vector beams: from mathematical concepts to applications," *Adv. Opt. Photonics* **1**(1), 1–57 (2009).
146. T. G. Brown, "Unconventional polarization states: beam propagation, focusing, and imaging," *Prog. Opt.* **56**, 81–129 (2011).
147. Z. Qiwen, *Vectorial Optical Fields: Fundamentals and Applications*, World Scientific, Singapore (2013).
148. J. Chen, C. Wan, and Q. Zhan, "Vectorial optical fields: recent advances and future prospects," *Sci. Bull.* **63**(1), 54–74 (2018).
149. H. Fujita, Y. Tada, and M. Sato, "Accessing electromagnetic properties of matter with cylindrical vector beams," *New J. Phys.* **21**, 073010 (2019).
150. N. K. Viswanathan and V. Inavalli, "Generation of optical vector beams using a two-mode fiber," *Opt. Lett.* **34**(8), 1189–1191 (2009).
151. V. K. Inavalli and N. K. Viswanathan, "Switchable vector vortex beam generation using an optical fiber," *Opt. Commun.* **283**(6), 861–864 (2010).
152. Y. Jayasurya, V. K. Inavalli, and N. K. Viswanathan, "Polarization singularities in the two-mode optical fiber output," *Appl. Opt.* **50**(25), E131–E137 (2011).
153. V. Kumar and N. K. Viswanathan, "The Pancharatnam–Berry phase in polarization singular beams," *J. Opt.* **15**(4), 044026 (2013).
154. A. M. Beckley, T. G. Brown, and M. A. Alonso, "Full Poincaré beams," *Opt. Express* **18**(10), 10777–10785 (2010).

155. C. Samlan et al., "Spin-orbit beams for optical Chirality measurement," *Appl. Phys. Lett.* **112**(3), 031101 (2018).
156. A. Forbes, A. Aiello, and B. Ndagano, "Classically entangled light," in *Progress in Optics*, T. Visser, Ed., pp. 99–153, Elsevier Ltd., Netherlands (2019).
157. K. Y. Bliokh et al., "Spin-orbit interactions of light," *Nat. Photonics* **9**(12), 796–808 (2015).
158. M. Berry and J. Hannay, "Umbilic points on Gaussian random surfaces," *J. Phys. A Math. Gen.* **10**(11), 1809–1821 (1977).
159. J. F. Nye, "Lines of circular polarization in electromagnetic wave fields," *Proc. R. Soc. Lond. A* **389**(1797), 279–290 (1983).
160. I. Freund, "Möbius strips and twisted ribbons in intersecting Gauss–Laguerre beams," *Opt. Commun.* **284**(16–17), 3816–3845 (2011).
161. B. Khajavi and E. Galvez, "High-order disclinations in space-variant polarization," *J. Opt.* **18**(8), 084003 (2016).
162. E. J. Galvez et al., "Generation of isolated asymmetric umbilics in light's polarization," *Phys. Rev. A* **89**(3), 031801 (2014).
163. J. F. Nye, *Natural Focusing and Fine Structure of Light: Caustics and Wave Dislocations*, CRC Press, Bristol (1999).
164. I. Freund, M. S. Soskin, and A. I. Mokhun, "Elliptic critical points in paraxial optical fields," *Opt. Commun.* **208**(4–6), 223–253 (2002).
165. M. Dennis, "Polarization singularities in paraxial vector fields: morphology and statistics," *Opt. Commun.* **213**(4–6), 201–221 (2002).
166. M. R. Dennis, K. O'Holleran, and M. J. Padgett, "Singular optics: optical vortices and polarization singularities," *Prog. Opt.* **53**, 293–363 (2009).
167. O. Angelsky et al., "Statistical and fractal structure of biological tissue Mueller matrix images," in *Optical Correlation: Techniques and Applications*, O. V. Angelsky, Ed., p. 213, SPIE Press, Bellingham, Washington, DC (2007).
168. J. Hajnal, "Singularities in the transverse fields of electromagnetic waves. I. theory," *Proc. R. Soc. Lond. A* **414**(1847), 433–446 (1987).
169. J. Hajnal, "Compound modulated scatterer measuring system," *IEE Proc. H-Microwaves, Antennas Propag.* **134**, 350–356 (1987).
170. J. Hajnal, "Observations of singularities in the electric and magnetic fields of freely propagating microwaves," *Proc. R. Soc. Lond. Ser. A* **430**(1879), 413–421 (1990).
171. M. S. Soskin, V. Denisenko, and I. Freund, "Optical polarization singularities and elliptic stationary points," *Opt. Lett.* **28**(16), 1475–1477 (2003).
172. R. Bhandari, "Polarization of light and topological phases," *Phys. Rep.* **281**(1), 1–64 (1997).
173. E. Hasman et al., "Chapter 4—space-variant polarization manipulation," in *Progress in Optics*, E. Wolf, Ed., vol. **47**, pp. 215–289, Elsevier, Netherlands (2005).
174. A. Niv et al., "Manipulation of the Pancharatnam phase in vectorial vortices," *Opt. Express* **14**(10), 4208–4220 (2006).
175. V. Kumar and N. K. Viswanathan, "Topological structures in the Poynting vector field: an experimental realization," *Opt. Lett.* **38**(19), 3886–3889 (2013).
176. F. Cardano et al., "Generation and dynamics of optical beams with polarization singularities," *Opt. Express* **21**(7), 8815–8820 (2013).
177. A. Volyar, T. Fadeeva, and Y. A. Egorov, "Vector singularities of Gaussian beams in uniaxial crystals: optical vortex generation," *Tech. Phys. Lett.* **28**(11), 958–961 (2002).
178. A. Volyar and T. Fadeeva, "Generation of singular beams in uniaxial crystals," *Opt. Spectrosc.* **94**(2), 235–244 (2003).
179. C. Samlan, D. N. Naik, and N. K. Viswanathan, "Isogyres-manifestation of spin-orbit interaction in uniaxial crystal: a closed-fringe Fourier analysis of conoscopic interference," *Sci. Rep.* **6**, 33141 (2016).
180. A. Ariyawansa, K. Liang, and T. G. Brown, "Polarization singularities in a stress-engineered optic," *J. Opt. Soc. Am. A* **36**(3), 312–319 (2019).
181. Z. Zhao et al., "Metamaterials-based broadband generation of orbital angular momentum carrying vector beams," *Opt. Lett.* **38**(6), 932–934 (2013).

182. Y. He et al., "Switchable phase and polarization singular beams generation using dielectric metasurfaces," *Sci. Rep.* **7**(1), 6814 (2017).
183. J. Wang and J. Du, "Metasurfaces for spatial light manipulation," in *Metamaterials: Devices and Applications*, p. 57 (2017).
184. A. de Hoogh et al., "Creating and controlling polarization singularities in plasmonic fields," in *Photonics*, Y. Kivshar, Ed., Vol. **2**, pp. 553–567, Multidisciplinary Digital Publishing Institute, Switzerland (2015).
185. C. Alpmann et al., "Dynamic modulation of Poincaré beams," *Sci. Rep.* **7**(1), 8076 (2017).
186. H. Rubinsztein-Dunlop et al., "Roadmap on structured light," *J. Opt.* **19**(1), 013001 (2016).
187. C. Rosales-Guzmán, B. Ndagano, and A. Forbes, "A review of complex vector light fields and their applications," *J. Opt.* **20**(12), 123001 (2018).
188. Y.-X. Ren, R.-D. Lu, and L. Gong, "Tailoring light with a digital micromirror device," *Ann. Phys.* **527**(7–8), 447–470 (2015).
189. D. Naidoo et al., "Controlled generation of higher-order Poincaré sphere beams from a laser," *Nat. Photonics* **10**(5), 327–332 (2016).
190. D. Li et al., "Generation of arbitrary perfect Poincaré beams," *J. Appl. Phys.* **125**(7), 073105 (2019).
191. R. Xu et al., "Perfect higher-order Poincaré sphere beams from digitalized geometric phases," *Phys. Rev. Appl.* **10**(3), 034061 (2018).
192. V. Kumar and N. K. Viswanathan, "Topological structures in vector-vortex beam fields," *J. Opt. Soc. Am. B* **31**(6), A40–A45 (2014).
193. M. P. Lavery et al., "Robust interferometer for the routing of light beams carrying orbital angular momentum," *N. J. Phys.* **13**(9), 093014 (2011).
194. E. Karimi et al., "Efficient generation and sorting of orbital angular momentum eigenmodes of light by thermally tuned Q-plates," *Appl. Phys. Lett.* **94**(23), 231124 (2009).
195. J. Leach et al., "Measuring the orbital angular momentum of a single photon," *Phys. Rev. Lett.* **88**(25), 257901 (2002).
196. C. Gao et al., "Sorting and detecting orbital angular momentum states by using a Dove prism embedded Mach–Zehnder interferometer and amplitude gratings," *Opt. Commun.* **284**(1), 48–51 (2011).
197. G. C. Berkhout et al., "Efficient sorting of orbital angular momentum states of light," *Phys. Rev. Lett.* **105**(15), 153601 (2010).
198. S. Lightman et al., "Miniature wide-spectrum mode sorter for vortex beams produced by 3D laser printing," *Optica* **4**(6), 605–610 (2017).
199. Y. Saito, S.-I. Komatsu, and H. Ohzu, "Scale and rotation invariant real time optical correlator using computer generated hologram," *Opt. Commun.* **47**(1), 8–11 (1983).
200. L. Allen and M. Padgett, "The Poynting vector in Laguerre–Gaussian beams and the interpretation of their angular momentum density," *Opt. Commun.* **184**(1–4), 67–71 (2000).
201. M. Rahm et al., "Optical design of reflectionless complex media by finite embedded coordinate transformations," *Phys. Rev. Lett.* **100**(6), 063903 (2008).
202. H. Zhou et al., "Tunable image rotator of light with optical geometric transformation," *IEEE Photonics J.* **8**(5), 1–7 (2016).
203. Y. Ren et al., "Atmospheric turbulence effects on the performance of a free space optical link employing orbital angular momentum multiplexing," *Opt. Lett.* **38**(20), 4062–4065 (2013).
204. G. Ruffato et al., "A compact diffractive sorter for high-resolution demultiplexing of orbital angular momentum beams," *Sci. Rep.* **8**, 10248 (2018).
205. C. Wan, J. Chen, and Q. Zhan, "Compact and high-resolution optical orbital angular momentum sorter," *APL Photonics* **2**(3), 031302 (2017).
206. R. Fickler, M. Ginoya, and R. W. Boyd, "Custom-tailored spatial mode sorting by controlled random scattering," *Phys. Rev. B* **95**(16), 161108 (2017).
207. Y. Wen et al., "Spiral transformation for high-resolution and efficient sorting of optical vortex modes," *Phys. Rev. Lett.* **120**(19), 193904 (2018).
208. C. Li and S. Zhao, "Efficient separating orbital angular momentum mode with radial varying phase," *Photonics Res.* **5**(4), 267–270 (2017).

209. G. Ruffato, M. Massari, and F. Romanato, "Compact sorting of optical vortices by means of diffractive transformation optics," *Opt. Lett.* **42**(3), 551–554 (2017).
210. J. Nicholson et al., "Spatially and spectrally resolved imaging of modal content in large-mode-area fibers," *Opt. Express* **16**(10), 7233–7243 (2008).
211. R. Brüning et al., "Comparative analysis of numerical methods for the mode analysis of laser beams," *Appl. Opt.* **52**(32), 7769–7777 (2013).
212. L. Huang et al., "Real-time mode decomposition for few-mode fiber based on numerical method," *Opt. Express* **23**(4), 4620–4629 (2015).
213. J. M. Andersen et al., "Characterizing vortex beams from a spatial light modulator with collinear phase-shifting holography," *Appl. Opt.* **58**(2), 404–409 (2019).
214. W. Yan, X. Xu, and J. Wang, "Modal decomposition for few mode fibers using the fractional Fourier system," *Opt. Express* **27**(10), 13871–13883 (2019).
215. T. Kaiser et al., "Complete modal decomposition for optical fibers using CGH-based correlation filters," *Opt. Express* **17**(11), 9347–9356 (2009).
216. G. Gibson et al., "Free-space information transfer using light beams carrying orbital angular momentum," *Opt. Express* **12**(22), 5448–5456 (2004).
217. L. Li et al., "Multimode fiber modal decomposition based on hybrid genetic global optimization algorithm," *Opt. Express* **25**(17), 19680–19690 (2017).
218. N. Bozinovic et al., "Control of orbital angular momentum of light with optical fibers," *Opt. Lett.* **37**(13), 2451–2453 (2012).
219. G. Xie et al., "Experimental demonstration of a 200-gbit/s free-space optical link by multiplexing Laguerre–Gaussian beams with different radial indices," *Opt. Lett.* **41**(15), 3447–3450 (2016).
220. S. Pachava, A. Dixit, and B. Srinivasan, "Modal decomposition of Laguerre Gaussian beams with different radial orders using optical correlation technique," *Opt. Express* **27**(9), 13182–13193 (2019).
221. J. George et al., "Beam quality degradation of a higher order transverse mode beam due to spherical aberration of a lens," *Appl. Opt.* **48**(32), 6202–6206 (2009).
222. A. Dixit, S. K. Mishra, and A. K. Gupta, "Sensitivity of singular beams in the presence of Zernike aberrations," *Opt. Lasers Eng.* **71**, 74–84 (2015).
223. S. Choudhary et al., "Measurement of the radial mode spectrum of photons through a phase-retrieval method," *Opt. Lett.* **43**(24), 6101–6104 (2018).
224. F. Bouchard et al., "Measuring azimuthal and radial modes of photons," *Opt. Express* **26**(24), 31925–31941 (2018).
225. D. Fu et al., "Realization of a scalable Laguerre–Gaussian mode sorter based on a robust radial mode sorter," *Opt. Express* **26**(25), 33057–33065 (2018).

Srinivas Pachava obtained his bachelor's degree in electronics and communications engineering from JNTU Kakinada in 2013 and his master's and PhD degrees from IIT Madras in June 2019. Currently, he is working as a postdoctoral fellow on LiDAR for autonomous vehicles at Ben-Gurion University of the Negev, Israel. His research interests include generation, propagation, and purity estimation of orbital angular momentum beams in both free-space and optical fiber.

Raghu Dharmavarapu received his bachelor's degree in electronics and communications engineering from JNTU Hyderabad in 2012 and a master's degree in electrical engineering from IIT Madras. Currently, he is a joint PhD student at Swinburne University of Technology working under the supervision of Prof. Saulius Juodkazis and Dr. Shanti Bhattacharya (IIT Madras). His PhD work is related to diffractive optical elements, dielectric metasurfaces for wavefront shaping, and complex light field generation.

Anand Vijayakumar received his PhD in optics from the Department of Electrical Engineering, IIT Madras (IIT-M) in 2015. He was a PBC postdoctoral fellow in the Electro Optics Research Group, Department of Electrical and Computer Engineering, Ben Gurion University of the Negev, Israel, from 2015–2018. Currently, he is a nanophotonics research fellow at the Center for Microphotonics, Swinburne University of Technology, Australia. His research interests include imaging, digital holography, diffractive optics, and nanophotonics.

Sruthy Jayakumar received her bachelor's degree in electronics communication from the University of Calicut in 2015. She is doing her master's in microelectronics and photonics in the Department of Electrical Engineering, IIT Madras. Her research interests are in the field of diffractive optical elements, generation of orbital angular momentum (OAM) beams and study of OAM beam propagation through scattering medium using compact diffractive elements

Amogh Manthalkar received his BTech in electronics and telecommunication engineering from SGGS Institute of Engineering and Technology under SRTM University, Nanded, Maharashtra in the year 2017. He is doing his master's in photonics in the Department of Electrical Engineering, IIT Madras. His research interests are diffractive optics using a digital micromirror device (DMD), generation of orbital angular momentum (OAM) beams and digital holography.

Awakash Dixit received his PhD in physics from DRDO-Instruments Research and Development Establishment/Uttarakhand Technical University, Dehradun, India, and MSc degree in electronics from UIET, CSJM University, Kanpur, India. Currently, he is working as a senior scientist at the Indian Institute of Technology Madras, Chennai, India. His areas of interest are singular optics, atmospheric turbulence, adaptive optics, lithography, micro-optics: design fabrication and characterization, and beam combining.

Nirmal K. Viswanathan received his PhD from the University of Hyderabad in 1997, where he is currently a professor in the School of Physics. He is a recipient of 3M Circle of Technical Excellence and Innovation (CTE & I) in Individual Technical Achievement award in 2001. He has an associate editor of *Optical Engineering* since 2017. His current research interests include singular optics, optical angular momentum, and spin-orbit interaction of light.

Balaji Srinivasan received his PhD from the University of New Mexico, USA, in 2000. He subsequently worked as a senior development scientist at Corning Incorporated, USA. Since 2004 he has been with the Indian Institute of Technology Madras as faculty in the Department of Electrical Engineering. His research interests span the development of active and passive optical components/subsystems for fiber lasers and distributed fiber optic sensors.

Shanti Bhattacharya received her PhD in physics from the Indian Institute of Technology, Madras, in 1997. She worked at the Darmstadt, Germany, first as an Alexander von Humboldt fellow and then as a guest scientist. Currently, she is a professor and has been with the Department of Electrical Engineering, IIT Madras, since 2005. Her present research interests are diffractive optics, optical MEMS and the development of measurement, and imaging techniques using fibre interferometry.